The Astrophysical Journal, 903:112 (28pp), 2020 November 10 https://doi.org/10.3847/1538-4357/abbc1c

The Sloan Digital Sky Survey Reverberation Mapping Project: Estimating Masses of Black Holes in Quasars with Single-epoch Spectroscopy

Elena Dalla Bontà[1,2], Bradley M. Peterson[3,4,5], Misty C. Bentz[6], W. N. Brandt[7,8,9], S. Ciroi[1], Gisella De Rosa[5], Gloria Fonseca Alvarez[10], Catherine J. Grier[11], P. B. Hall[12], Juan V. Hernández Santisteban[13], Luis C. Ho[14,15], Y. Homayouni[16], Keith Horne[13], C. S. Kochanek[3,4], Jennifer I-Hsiu Li[17], L. Morelli[2,18], A. Pizzella[1,2], R. W. Pogge[3,4], D. P. Schneider[7,8], Yue Shen[17,19,21], J. R. Trump[10], and Marianne Vestergaard[11,20]
[1] Dipartimento di Fisica e Astronomia "G. Galilei," Università di Padova, Vicolo dell'Osservatorio 3, I-35122 Padova, Italy
[2] INAF-Osservatorio Astronomico di Padova, Vicolo dell'Osservatorio 5, I-35122, Padova, Italy
[3] Department of Astronomy, The Ohio State University, 140 W. 18th Avenue, Columbus, OH 43210, USA
[4] Center for Cosmology and AstroParticle Physics, 191 Woodruff Avenue, Columbus, OH 43210, USA
[5] Space Telescope Science Institute, 3700 San Martin Drive, Baltimore, MD 21218, USA
[6] Department of Physics and Astronomy, Georgia State University, 25 Park Place, Suite 605, Atlanta, GA 30303, USA
[7] Department of Astronomy and Astrophysics, Eberly College of Science, The Pennsylvania State University, 525 Davey Laboratory, University Park, PA 16802, USA
[8] Institute for Gravitation and the Cosmos, The Pennsylvania State University, University Park, PA 16802, USA
[9] Department of Physics, The Pennsylvania State University, 525 Davey Laboratory, University Park, PA 16802, USA
[10] Department of Physics, University of Connecticut, 2152 Hillside Road, Unit 3046, Storrs, CT 06269, USA
[11] Steward Observatory, University of Arizona, 933 North Cherry Avenue, Tucson, AZ 85721, USA
[12] Department of Physics and Astronomy, York University, Toronto, ON M3J 1P3, Canada
[13] SUPA Physics and Astronomy, University of St. Andrews, Fife, KY16 9SS, UK
[14] Kavli Institute for Astronomy and Astrophysics, Peking University, Beijing 100871, People's Republic of China
[15] Department of Astronomy, School of Physics, Peking University, Beijing 100871, People's Republic of China
[16] Department of Physics, University of Connecticut, 2152 Hillside Road, Unit 3046, Storrs, CT 06269-3046, USA
[17] Department of Astronomy, University of Illinois at Urbana–Champaign, Urbana, IL 61801, USA
[18] Instituto de Astronomìa y Ciencias Planetarias, Universidad de Atacama, Copayapu 485, Copiapò, Chile
[19] National Center for Supercomputing Applications, University of Illinois at Urbana-Champaign, Urbana, IL 61801, USA
[20] DARK, Niels Bohr Institute, University of Copenhagen, Jagtvej 128, DK-2200 Copenhagen, Denmark
Received 2020 July 5; revised 2020 September 22; accepted 2020 September 25; published 2020 November 9

Abstract

It is well known that reverberation mapping of active galactic nuclei (AGNs) reveals a relationship between AGN luminosity and the size of the broad-line region, and that use of this relationship, combined with the Doppler width of the broad emission line, enables an estimate of the mass of the black hole at the center of the active nucleus based on a single spectrum. An unresolved key issue is the choice of parameter used to characterize the line width, either FWHM or line dispersion $\sigma_{\rm line}$ (the square root of the second moment of the line profile). We argue here that use of FWHM introduces a bias, stretching the mass scale such that high masses are overestimated and low masses are underestimated. Here we investigate estimation of black hole masses in AGNs based on individual or "single-epoch" observations, with a particular emphasis in comparing mass estimates based on line dispersion and FWHM. We confirm the recent findings that, in addition to luminosity and line width, a third parameter is required to obtain accurate masses, and that parameter seems to be Eddington ratio. We present simplified empirical formulae for estimating black hole masses from the Hβ λ4861 and C IV λ1549 emission lines. While the AGN continuum luminosity at 5100 Å is usually used to predict the Hβ reverberation lag, we show that the luminosity of the Hβ broad component can be used instead without any loss of precision, thus eliminating the difficulty of accurately accounting for the host-galaxy contribution to the observed luminosity.

Unified Astronomy Thesaurus concepts: Active galactic nuclei (16); Quasars (1319); Supermassive black holes (1663)

1. Introduction

1.1. Reverberation-based Black Hole Masses

The presence of emission lines with Doppler widths of thousands of kilometers per second is one of the defining characteristics of active galactic nuclei (AGNs; Burbidge & Burbidge 1967; Weedman 1976). It was long suspected that the large line widths were due to motions in a deep gravitational potential and that this implied very large central masses (e.g., Woltjer 1959), as did the Eddington limit (Tarter & McKee 1973). Under a few assumptions, the central mass is $M \propto V^2R$, where V is the Doppler width of the line and R is the size of the broad-line region (BLR). It is the latter quantity that is difficult to determine. An early attempt to estimate R by Dibai (1980) was based on the assumption of constant emissivity per unit volume but led to an incorrect dependence on luminosity, as in this case luminosity is proportional to volume, so $R \propto L^{1/3}$. Wandel & Yahil (1985) inferred the BLR size from the Hβ luminosity. Other attempts were based on photoionization physics (see Ferland & Shields 1985; Osterbrock 1985). Davidson (1972) found that the relative

[21] Alfred P. Sloan Research Fellow.

strength of emission lines in ionized gas could be characterized by an ionization parameter

$$U = \frac{Q(\mathrm{H})}{4\pi R^2 c n_{\mathrm{H}}}, \quad (1)$$

where Q(H) is the rate at which H-ionizing photons are emitted by the central source and n_{H} is the particle density of the gas. The ionization parameter U is proportional to the ratio of ionization rate to recombination rate in the BLR clouds. The similarity of emission-line flux ratios in AGN spectra over orders of magnitude in luminosity suggested that U is constant, and the presence of C III] λ1909 sets an upper limit on the density $n_{\mathrm{H}} \lesssim 10^{9.5}$ cm^{-3} (Davidson & Netzer 1979). Since $L \propto Q(\mathrm{H})$, this naturally led to the prediction that the BLR radius would scale with luminosity as $R \propto L^{1/2}$. Unfortunately, best-estimate values for Q(H) and n_{H} led to a significant overestimate of the BLR radius (Peterson et al. 1985) as a consequence of the simple but erroneous assumption that all the broad lines arise cospatially (i.e., models employed a single representative BLR cloud).

With the advent of reverberation mapping (hereafter RM; Blandford & McKee 1982; Peterson 1993), direct measurements of R enabled improved black hole mass determinations. Attempts to estimate black hole masses based on early RM results and the $R \propto L^{1/2}$ prediction included those of Padovani & Rafanelli (1988), Koratkar & Gaskell (1991), and Laor (1998). The first multiwavelength RM campaigns demonstrated ionization stratification of the BLR (Clavel et al. 1991; Krolik et al. 1991; Peterson et al. 1991), and this eventually led to identification of the virial relationship, $R \propto V^{-2}$ (Peterson & Wandel 1999, 2000; Onken & Peterson 2002; Kollatschny 2003; Bentz et al. 2010), which gave reverberation-based mass measurements higher levels of credibility. Of course, the virial relationship demonstrates only that the central force has an R^{-2} dependence, which is also characteristic of radiation pressure; whether or not radiation pressure from the continuum source is important has not been clearly established (Marconi et al. 2008, 2009; Netzer & Marziani 2010). If radiation pressure in the BLR turns out to be important, then the black hole masses, as we discuss them here, are underestimated.

Masses of AGN black holes are computed as

$$M_{\mathrm{BH}} = f\left(\frac{V^2 R}{G}\right), \quad (2)$$

where V is the line width, R is the size of the BLR from the reverberation lag, and G is the gravitational constant. The quantity in parentheses is often referred to as the virial product μ; it incorporates the two observables in RM, line width and time delay $\tau = R/c$, and is in units of mass. The scaling factor f is a dimensionless quantity of order unity that depends on the geometry, kinematics, and inclination of the AGN. Throughout most of this work, we ignore f (i.e., set it to unity) and work strictly with the virial product.

While RM has emerged as the most effective technique for measuring the black hole masses in AGNs (Peterson 2014), it is resource intensive, requiring many observations over an extended period of time at fairly high cadence. Fortunately, observational confirmation of the R–L relationship (Kaspi et al. 2000, 2005; Bentz et al. 2006b, 2009a, 2013) enables "single-epoch" mass estimates because, in principle, a single spectrum could yield V and also R, through measurement of L (e.g., Wandel et al. 1999; McLure & Jarvis 2002; Vestergaard 2002, 2004; Corbett et al. 2003; Kollmeier et al. 2006; Vestergaard & Peterson 2006; Fine et al. 2008; Shen et al. 2008a, 2008b; Vestergaard et al. 2008). Of the three strong emission lines generally used to estimate central black hole masses, the R–L relationship is only well established for Hβ λ4861 (Bentz et al. 2013 and references therein; but see the discussion in Section 3.3). Empirically establishing the R–L relationship for Mg II λ2798 (Clavel et al. 1990, 1991; Reichert et al. 1994; Metzroth et al. 2006; Cackett et al. 2015; Shen et al. 2016; Lira et al. 2018; Czerny et al. 2019; Homayouni et al. 2020; Zajaček et al. 2020), as well as for C IV λ1549 (Clavel et al. 1989, 1990, 1991; Reichert et al. 1994; Korista et al. 1995; Rodríguez-Pascual et al. 1997; Wanders et al. 1997; O'Brien et al. 1998; Peterson et al. 2005; Metzroth et al. 2006; Kaspi et al. 2007; Trevese et al. 2014; De Rosa et al. 2015; Lira et al. 2018; Grier et al. 2019; Hoormann et al. 2019), has been difficult because of the nature of the UV line variability and the high level of competition for suitable facilities.

Masses based on the C IV λ1549 emission line, in particular, have been somewhat controversial. Some studies claim that there is good agreement between masses based on C IV and those measured from other lines (Vestergaard & Peterson 2006; Greene et al. 2010; Assef et al. 2011). On the other hand, there are several claims that there is inadequate agreement with masses based on other emission lines (Baskin & Laor 2005; Netzer et al. 2007; Sulentic et al. 2007; Shen et al. 2008b; Shen & Liu 2012; Trakhtenbrot & Netzer 2012). Denney et al. (2009a, 2013), however, note that there are a number of biases that can adversely affect single-epoch mass estimates, with low signal-to-noise ratio (S/N) "survey quality" data being an important problem with some of the studies for which poor agreement between C IV and other lines is found. It has also been argued, however, that some fitting methodologies are more affected by this than others (Shen et al. 2019). There have been more recent papers that attempt to correct C IV mass determinations to better agree with those based on other lines (e.g., Bian et al. 2012; Runnoe et al. 2013a; Brotherton et al. 2015a; Coatman et al. 2017; Mejía-Restrepo et al. 2018; Marziani et al. 2019).

1.2. Characterizing Line Widths

As first shown by Denney et al. (2009a) and Denney (2012), the apparent difficulties with C IV-based masses trace back not only to the S/N issue but also to how the line widths are characterized. It has been customary in AGN studies to characterize line widths by one of two parameters, either FWHM or the line dispersion σ_{line}, which is defined by

$$\sigma_{\mathrm{line}} = \left[\frac{\int(\lambda - \lambda_0)^2 P(\lambda) d\lambda}{\int P(\lambda) d\lambda}\right]^{1/2}, \quad (3)$$

where $P(\lambda)$ is the emission-line profile as a function of wavelength and λ_0 is the line centroid,

$$\lambda_0 = \frac{\int \lambda P(\lambda) d\lambda}{\int P(\lambda) d\lambda}. \quad (4)$$

While both FWHM and σ_{line} have been used in the virial equation to estimate AGN black hole masses, they are not

interchangeable. It is well known that AGN line profiles depend on the line width (Joly et al. 1985): broader lines have lower kurtosis, i.e., they are "boxier" rather than "peakier." Indeed, for AGNs, the ratio FWHM/$\sigma_{\rm line}$ has been found to be a simple but useful characterization of the line profile (Collin et al. 2006; Kollatschny & Zetzl 2013).

Each line-width measure has practical strengths and weaknesses (Peterson et al. 2004; Wang et al. 2020). The line dispersion $\sigma_{\rm line}$ is more physically intuitive, but it is sensitive to the line wings, which are often badly blended with other features. All three of the strong lines usually used to estimate masses—Hβ λ4861, Mg II λ2798, and C IV λ1549—are blended with other features: the Fe II λ4570 and Fe II $\lambda\lambda$5190, 5320 complexes (Phillips 1978) and He II λ4686 in the case of Hβ, the UV Fe II complexes in the case of Mg II, and He II λ1640 in the case of C IV. The red wing of the Hβ line is also blended with [O III] $\lambda\lambda$4959, 5007, although because they do not vary on short timescales, these narrow lines disappear in the rms spectrum (defined below) and, on account of their narrowness, can usually be removed from mean or single spectra as we note below. The FWHM can usually be measured more precisely than $\sigma_{\rm line}$ (although Peterson et al. 2004 note that the opposite is true for the rms spectra, which are sometimes quite noisy), but it is not clear that FWHM yields more *accurate* mass measurements. In practice, FWHM is used more often than $\sigma_{\rm line}$ because it is relatively simple to measure and can be measured more precisely, while $\sigma_{\rm line}$ often requires deblending or modeling the emission features, which does not necessarily yield unambiguous results.

There are, however, a number of reasons to prefer $\sigma_{\rm line}$ to FWHM as the line-width measure for estimating AGN black hole masses. Certainly for radio-loud AGNs, where inclination can be estimated from radio jets, core versus lobe dominance, or radio spectral index, it is well known that FWHM correlates with inclination (Wills & Browne 1986; Runnoe et al. 2013b; Brotherton et al. 2015b). Fromerth & Melia (2000) point out that $\sigma_{\rm line}$ better characterizes an arbitrary or irregular line profile. Peterson et al. (2004) note that $\sigma_{\rm line}$ produces a tighter virial relationship than FWHM, and Denney et al. (2013) find better agreement between C IV-based and Hβ-based mass estimates by using $\sigma_{\rm line}$ rather than FWHM (the latter two are essentially the same argument). In the case of NGC 5548, for which there are multiple reverberation-based mass measures, a possible correlation with luminosity is stronger for FWHM-based masses than for $\sigma_{\rm line}$-based masses, suggesting that the former are biased, as the same mass should be recovered regardless of the luminosity state of the AGN (Collin et al. 2006; Shen & Kelly 2012). A possibly more compelling argument for using $\sigma_{\rm line}$ instead of FWHM is bias in the mass scale that is introduced by using FWHM as the line width. Steinhardt & Elvis (2010) used single-epoch masses for more than 60,000 Sloan Digital Sky Survey (SDSS) quasars (Shen et al. 2008b) with masses computed using FWHM. They found that, in any redshift bin, if one plots the distribution of mass versus luminosity, the higher-mass objects lie increasingly below the Eddington limit; they refer to this as the "sub-Eddington boundary." There is no physical basis for this. Rafiee & Hall (2011) point out, however, that if the quasar masses are computed using $\sigma_{\rm line}$ instead of FWHM, the sub-Eddington boundary disappears: the distribution of quasar black hole masses approaches the Eddington limit at all masses. Referring to Figure 1 of Rafiee & Hall (2011), the distribution of quasars in the mass versus luminosity diagram is an elongated cloud of points whose axis is roughly parallel to the Eddington ratio when $\sigma_{\rm line}$ is used to characterize the line width. However, when FWHM is used, the axis of the distribution rotates as the higher masses are underestimated and the lower masses are overestimated. However, the apparent rotation of the mass distribution is in the same sense that is expected from the Malmquist bias and a bottom-heavy quasar mass function (Shen 2013). Unfortunately, these arguments are not statistically compelling. Examination of the $M_{\rm BH}$–σ^* relation using FWHM-based and $\sigma_{\rm line}$-based masses is equally unrevealing (Wang et al. 2019).

In RM, a further distinction among line-width measures must be drawn since either FWHM or $\sigma_{\rm line}$ can be measured in the mean spectrum,

$$\overline{F}(\lambda) = \frac{1}{N}\sum_{1}^{N} F_i(\lambda), \tag{5}$$

where $F_i(\lambda)$ is the flux in the ith spectrum of the time series at wavelength λ and N is the number of spectra, or they can be measured in the rms residual spectrum (hereafter simply "rms spectrum"), which is defined as

$$\sigma_{\rm rms}(\lambda) = \left\{\frac{1}{N-1}\sum_{1}^{N}[F_i(\lambda) - \overline{F}(\lambda)]^2\right\}^{1/2}. \tag{6}$$

In this paper, we will specifically refer to the measurements of $\sigma_{\rm line}$ in the mean spectrum as $\sigma_{\rm M}$ and in the rms spectrum as $\sigma_{\rm R}$. Similarly, FWHM$_{\rm M}$ refers to FWHM of a line in the mean spectrum or a single-epoch spectrum, and FWHM$_{\rm R}$ is the FWHM in the rms spectrum. It is common to use $\sigma_{\rm R}$ as the line-width measure for determining black hole masses from reverberation data—it is intuitively a good choice, as it isolates the gas in the BLR that is actually responding to the continuum variations. As noted previously, the strong and strongly variable broad emission lines can be hard to isolate, as they are blended with other features. In the rms spectra, however, the contaminating features are much less of a problem because they are generally constant or vary either slowly or weakly and thus nearly disappear in the rms spectra.

Since the goal is to measure a black hole mass from a single spectrum (or a few spectra), we must use a proxy for $\sigma_{\rm R}$. Here we will attempt to determine whether either $\sigma_{\rm M}$ or FWHM$_{\rm M}$ in a single or mean spectrum can serve as a suitable proxy for $\sigma_{\rm R}$; we know a priori that there are good, but nonlinear, correlations between $\sigma_{\rm R}$ and both $\sigma_{\rm M}$ and FWHM$_{\rm M}$. It therefore seems likely that either $\sigma_{\rm M}$ or FWHM$_{\rm M}$ could be used as a proxy for $\sigma_{\rm R}$.

Investigation of the relationship among the line-width measures motivated a broader effort to produce easy-to-use prescriptions for computing *accurate* black hole masses using Hβ and C IV emission lines and nearby continuum flux measurements for each line. We do not discuss Mg II RM results in this contribution, as the present situation has been addressed rather thoroughly by Bahk et al. (2019), Martínez-Aldama et al. (2020), and Homayouni et al. (2020). In Section 2, the data used in this investigation are described. In Section 3, the relationship between the Hβ reverberation lag and different measures of the AGN luminosity are considered, and we identify the physical parameters to lead to accurate black hole mass determinations. In Section 4, we will similarly discuss masses based on C IV. In Section 5, we present simple

empirical formulae for estimating black hole masses from Hβ or C IV; we regard this as the most important result of this study. The results of this investigation and our future plans to improve this method are outlined in Section 6. Our results are briefly summarized in Section 7. Throughout this work, we assume $H_0 = 72\,\mathrm{km\,s^{-1}\,Mpc^{-1}}$, $\Omega_{\mathrm{matter}} = 0.3$, and $\Omega_\Lambda = 0.7$.

2. Observational Database and Methodology

2.1. Data

We use two high-quality databases for this investigation:

1. Spectra and measurements for previously reverberation-mapped AGNs, for Hβ (Table A1) and for C IV (Table A2). These are mostly taken from the literature (see also Bentz & Katz 2015 for a compilation[22]). Sources without estimates of host-galaxy contamination to the optical luminosity L(5100 Å) have been excluded. This database provides the fundamental R–L calibration for the single-epoch mass scale. In this contribution, we will refer to these collectively as the "reverberation-mapping database (RMDB)."
2. Spectral measurements from the SDSS Reverberation Mapping Project (Shen et al. 2015; hereafter "SDSS-RM," or, more compactly, simply "SDSS"). We use both Hβ (Table A3) and C IV (Table A4) data from the 2014–2018 SDSS-RM campaign (Grier et al. 2017b, 2019; Shen et al. 2019). Each spectrum is composed of the average of the individual spectra obtained for each of the 849 quasars in the SDSS-RM field.

In addition, because C IV RM measurements remain rather scarce, we augmented the C IV sample with measurements from Vestergaard & Peterson (2006, hereafter VP06), who combined single-epoch luminosity and line-width measurements from archival UV spectra with Hβ-based mass measurements of the objects in Table A1. The UV parameters are given in Table A5; we note, however, that we have excluded 3C 273 and 3C 390.3 because they both have uncertainties in their virial product larger than 0.5 dex; the former was a particular problem because there were far more measurements of UV parameters for this source than for any other and the combination of a large number of measurements and a poorly constrained virial product conspired to disguise real correlations.

All SDSS-RM spectra have been reduced and processed as described by Shen et al. (2015, 2016), including post-processing with `PrepSpec` (K. Horne 2020, in preparation). We note that only lags (τ), line dispersion in the rms spectrum (σ_{R}), and virial products ($\mu_{\mathrm{RM}} = \sigma_{\mathrm{R}}^2 c\tau/G$) are taken from Grier et al. (2017b, 2019); all luminosities and other line-width measures are from Shen et al. (2019) (Tables A3 and A4 are included here for the sake of clarity).

For each SDSS AGN, there are two determinations of both $\mathrm{FWHM_M}$ and σ_{M}; one is the best fit (BF) to the mean spectrum, and the other is the mean of multiple Monte Carlo (MC) realizations. For each MC realization, N independent random selections of the N spectra are combined, and the line width is measured for both $\mathrm{FWHM_M}$ and σ_{M}. After a large number of realizations, the mean $\langle V\rangle$ and rms ΔV for $V = \mathrm{FWHM_M}$ and $V = \sigma_{\mathrm{M}}$ are computed, and the rms values are adopted as the uncertainties in each line-width measure.

[22] The database is regularly updated at http://www.astro.gsu.edu/AGNmass.

Table 1
Effects of Quality Cuts on SDSS-RM Sample Size

Criterion	Hβ	C IV
Original sample	221	540
(a) Minimum line width (Equation (7))	199	520
(b) Consistency (Equation (8))	194	368
(c) S/N (Equation (9))	121	462
(a) + (b)	174	352
(a) + (c)	108	450
(b) + (c)	107	309
(a) + (b) + (c)	96	299
All + BAL removal	96	248

For the purpose of mass estimation, we need to establish relationships based on the most reliable data. Many of the SDSS average spectra are still quite noisy, so we imposed quality cuts. Even though we are for the most part restricting our attention to the SDSS-RM quasars for which there are measured lags for Hβ (44 quasars) or C IV (48 quasars), we impose these cuts on the entire sample for the sake of later discussion. The first quality condition is that

$$V \geqslant 1000\,\mathrm{km\,s^{-1}} \tag{7}$$

for both $V = \mathrm{FWHM_M}$ and $V = \sigma_{\mathrm{M}}$, since AGNs with lines narrower than $1000\,\mathrm{km\,s^{-1}}$ are probably type 2 AGNs; there are some type 1 AGNs with line widths narrower than this, including several in Table A1, but these are low-luminosity AGNs (e.g., Greene & Ho 2007), not SDSS quasars. The second quality condition is that the best-fit value V(BF) must lie in the range

$$\langle V\rangle - \Delta V \leqslant V\,(\mathrm{BF}) \leqslant \langle V\rangle + \Delta V \tag{8}$$

for both FWHM and σ_{line}. A third quality condition is an S/N requirement that the line width must be significantly larger than its uncertainty. Some experimentation showed that

$$\frac{V}{\Delta V} \geqslant 10 \tag{9}$$

is a good criterion for both $V = \mathrm{FWHM_M}$ and $V = \sigma_{\mathrm{M}}$ to remove the worst outliers from the line-width comparisons discussed in Sections 3.2 and 4.1.

Finally, we removed quasars that were flagged by Shen et al. (2019) as having broad absorption lines (BALs), mini-BALs, or suspected BALs in C IV.

The effect of each quality cut on the size of the database available for each emission line is shown in Table 1. Of the 44 SDSS-RM quasars with measured Hβ lags, 12 failed to meet at least one of the quality criteria, usually the S/N requirement, thus reducing the SDSS-RM Hβ sample to 32 quasars. Three quasars with C IV reverberation measurements (RMID 362, 408, and 722) were rejected for significant BALs, thus reducing the SDSS-RM C IV reverberation sample to 45 quasars. As we will show in Section 5, another effect of imposing quality cuts is, not surprisingly, that it removes some of the lower-luminosity sources from the sample.

2.2. Fitting Procedure

Throughout this work, we use the fitting algorithm described by Cappellari et al. (2013) that combines the Least Trimmed Squares technique of Rousseeuw & van Driessen (2006) and a

least-squares fitting algorithm that allows errors in all variables and includes intrinsic scatter, as implemented by Dalla Bontà et al. (2018). Briefly, the fits we perform here are of the general form

$$y = a + b(x - x_0), \tag{10}$$

where x_0 is the median value of the observed parameter x. The fit is done iteratively with 5σ rejection (unless stated otherwise), and the best fit minimizes the quantity

$$\chi^2 = \sum_{i=1}^{N} \frac{[a + b(x_i - x_0) - y_i]^2}{(b\Delta x_i)^2 + (\Delta y_i)^2 + \varepsilon_y^2}, \tag{11}$$

where Δx_i and Δy_i are the errors on the variables x_i and y_i, and ε_y is the sigma of the Gaussian describing the distribution of intrinsic scatter in the y coordinate; ε_y is iteratively adjusted so that the χ^2 per degree of freedom $\nu = N - 2$ has the value of unity expected for a good fit. The observed scatter is

$$\Delta = \left\{ \frac{1}{N-2} \sum_{i=1}^{N} [y_i - a - b(x_i - x_0)]^2 \right\}^{1/2}. \tag{12}$$

The value of ε_y is added in quadrature when y is used as a proxy for x.

The bivariate fits are intended to establish the physical relationships among the various parameters and also to fit residuals. The actual mass estimation equations that we use will be based on multivariate fits of the general form

$$z = a + b(x - x_0) + c(y - y_0), \tag{13}$$

where the parameters are as described above, plus an additional observed parameter y that has median value y_0. Similarly to linear fits, the plane fitting minimizes the quantity

$$\chi^2 = \sum_{i=1}^{N} \frac{[a + b(x_i - x_0) + c(y_i - y_0) - z_i]^2}{(b\Delta x_i)^2 + (c\Delta y_i)^2 + (\Delta z_i)^2 + \varepsilon_z^2}, \tag{14}$$

with Δx_i, Δy_i, and Δz_i as the errors on the variables (x_i, y_i, z_i), and ε_z as the sigma of the Gaussian describing the distribution of intrinsic scatter in the z coordinate; ε_z is iteratively adjusted so that the χ^2 per degrees of freedom $\nu = N - 3$ has the value of unity expected for a good fit. The observed scatter is

$$\Delta = \left\{ \frac{1}{N-3} \sum_{i=1}^{N} [z_i - a - b(x_i - x_0) - c(y_i - y_0)]^2 \right\}^{1/2}. \tag{15}$$

3. Masses Based on Hβ

3.1. The R–L Relationships

In this section, we examine the calibration of the fundamental Hβ *R–L* relationship using various luminosity measures. The analysis in this section is based only on the RMDB sample in Table A1 because all these sources have been corrected for host-galaxy starlight. To obtain accurate masses from Hβ, contaminating starlight from the host galaxy must be accounted for in the luminosity measurement, or the mass will be overestimated. For reverberation-mapped sources, this has been done by modeling unsaturated images of the AGNs obtained with the Hubble Space Telescope (HST; Bentz et al. 2006b, 2009a, 2013). The AGN contribution was removed from each image by modeling the images as an extended host galaxy plus a central point source representing the AGN. The starlight contribution to the RM spectra is determined by using simulated aperture photometry of the AGN-free image. In panel (a) of Figure 1, we show the Hβ lag as a function of the AGN continuum with the host contribution removed in each case. This essentially reproduces the result of Bentz et al. (2013), as small differences are due solely to improvements in the quality and quantity of the RM database (see Table A1); we give the best-fit values to Equation (10) in the first line of Table 2.

Accounting for the host-galaxy contribution in the same way for a large number of AGNs, such as those in SDSS-RM (not to mention the entire SDSS catalog), is simply not feasible. It is well known, however, that there is a tight correlation between the AGN continuum luminosity and the luminosity of Hβ (e.g., Yee 1980; Ilić et al. 2017), and it has indeed been argued that the Hβ emission-line luminosity can be used as a proxy for the AGN continuum luminosity for reverberation studies (Kaspi et al. 2005; Vestergaard & Peterson 2006; Greene et al. 2010). However, in some of the reverberation-mapped sources, narrow-line Hβ contributes significantly to the total Hβ flux; NGC 4151 is an extreme example (e.g., Antonucci & Cohen 1983; Bentz et al. 2006a; Fausnaugh et al. 2017). Whenever the narrow-line component can be isolated, it has been subtracted from the total Hβ flux. This also affects the line-width measurements. In general, it is assumed that [O III] λ5007 can be used as a template for narrow Hβ. The template is shifted and scaled to the largest flux that, when subtracted from the spectrum, does not produce a depression at the center of the remaining broad Hβ component. In Figure 2, we show the tight relationship between $L_{\rm AGN}(5100\,\text{Å})$ and $L(\text{H}\beta_{\rm broad})$; the best-fit coefficients for this relationship are given in Table 2.

In panel (b) of Figure 1, we show the Hβ lag as a function of the luminosity of the broad component of Hβ, with the narrow component removed whenever possible. We give the best-fit values to Equation (10) in the second row of Table 2, which shows that the slope of this relationship is nearly identical to the slope of the *R–L* relationship using the AGN continuum. The luminosity of the Hβ broad component is thus an excellent proxy for the AGN luminosity and requires only removal of the Hβ narrow component (at least when it is significant), which is much easier than estimating the starlight contribution to the continuum luminosity at 5100 Å. Moreover, by using the line flux instead of the continuum flux, we can include core-dominated radio sources where the continuum may be enhanced by the jet component (Greene & Ho 2005). This is therefore the *R–L* relationship we prefer for the purpose of estimating single-epoch masses, and we will focus on this relationship throughout the remainder of this contribution.

3.2. Line-width Relationships

We now consider the use of $\sigma_{\rm M}$ and $\text{FWHM}_{\rm M}$ as proxies for $\sigma_{\rm R}$ (see Collin et al. 2006; Wang et al. 2019). Panel (a) of Figure 3 shows the relationship between $\sigma_{\rm R}(\text{H}\beta)$, the H$\beta$ line dispersion in the rms spectrum, and $\sigma_{\rm M}(\text{H}\beta)$, the H$\beta$ line dispersion in the mean spectrum. The relationship is nearly linear (slope $= 1.085 \pm 0.045$), and the intrinsic scatter is small (0.079 dex). The fit coefficients are given in the first line of Table 3.

We also show in panel (a) of Figure 3 the relationship between $\sigma_{\rm R}(\text{H}\beta)$ and the FWHM of Hβ in the mean spectrum,

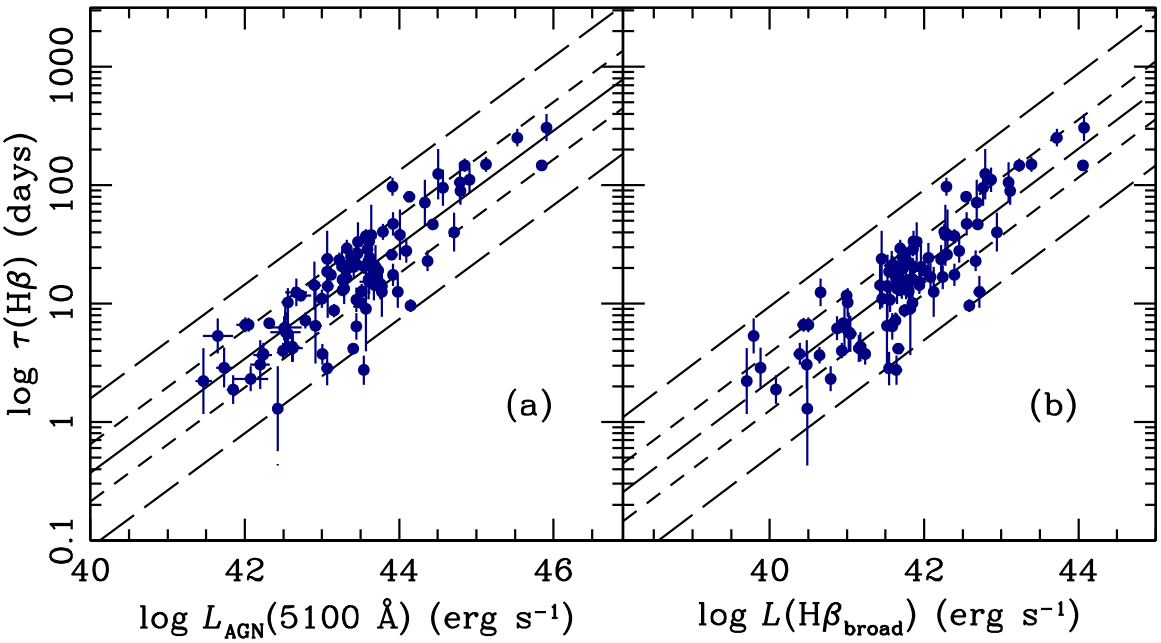

Figure 1. (a) Rest-frame Hβ lag in days as a function of the AGN luminosity $L_{\rm AGN}$(5100 Å) in erg s^{-1}. The host-galaxy starlight contribution has been removed by using unsaturated HST images (see Bentz et al. 2013). (b) Hβ lag in days as a function of the broad Hβ luminosity L(H$\beta_{\rm broad}$) in erg s^{-1}. The narrow component of Hβ has been removed in each case where it was sufficiently strong (i.e., easily identifiable) to isolate. In both panels, the solid line shows the best fit to the data using Equation (10), with coefficients given in Table 2. The short-dashed lines show the $\pm1\sigma$ uncertainty (equivalent to enclosing 68% of the values for a Gaussian distribution), and the long-dashed lines show the 2.6σ uncertainties (equivalent to enclosing 99% of the values for a Gaussian distribution). The Spearman rank correlation coefficient for the data in panel (a) is $\rho = 0.797$, and the probability that the relationship arises by chance is $P < 10^{-6}$, and for the data in panel (b), $\rho = 0.873$ with $P < 10^{-6}$.

FWHM$_{\rm M}$(Hβ). The fit coefficients are given in the second line of Table 3. The relationship is far from linear (slope $=$ 0.535 ± 0.042), and the scatter ε_y is larger than it is for the $\sigma_{\rm R}$(Hβ)–$\sigma_{\rm M}$(Hβ) relationship, even after removal of the notable outliers. The shallow slope of the relationship between FWHM$_{\rm M}$ and $\sigma_{\rm R}$ is why the mass distribution is stretched by using FWHM$_{\rm M}$ as the line-width measure in Equation (2): for any given R, the ratio (FWHM$_{\rm M}/\sigma_{\rm R}$)^2 is larger at the high-mass end of the distribution than it is at the low-mass end. Use of FWHM$_{\rm M}$ in Equation (2) overestimates the high masses and underestimates the low masses. While it is clear that $\sigma_{\rm M}$(Hβ) is an excellent proxy for $\sigma_{\rm R}$(Hβ), the value of FWHM$_{\rm M}$(Hβ) is less clear, though the shallow slope of the FWHM$_{\rm M}$–$\sigma_{\rm R}$ relationship needs to be taken into account. We will fit both versions in order to understand the relative merits of each.

3.3. Single-epoch Predictors of the Virial Product

In the previous subsections, we have reestablished the correlations between τ(Hβ) and L(H$\beta_{\rm broad}$) and between $\sigma_{\rm R}$(Hβ) and both $\sigma_{\rm M}$(Hβ) and FWHM$_{\rm M}$(Hβ). As a first approximation for a formula to estimate single-epoch masses, we fit the following equations:

$$\log \mu_{\rm RM}({\rm H}\beta) = a + b[\log L({\rm H}\beta_{\rm broad}) - x_0] + c[\log \sigma_{\rm M}({\rm H}\beta) - y_0], \quad (16)$$

and

$$\log \mu_{\rm RM}({\rm H}\beta) = a + b[\log L({\rm H}\beta_{\rm broad}) - x_0] + c[\log {\rm FWHM_M}({\rm H}\beta) - y_0]. \quad (17)$$

The results of these fits based on the combined RMDB data (Table A1) and SDSS data (Table A3) are given in the first two lines of Table 4 and illustrated in panels (a) and (b) of Figure 4.

Using these coefficients, we have initial predictors of $\log \mu_{\rm SE}$(Hβ) using $\sigma_{\rm M}$ as the line-width measure,

$$\log \mu_{\rm SE}({\rm H}\beta) = 6.975 + 0.566[\log L({\rm H}\beta_{\rm broad}) - 41.857] + 1.757[\log \sigma_{\rm M}({\rm H}\beta) - 3.293], \quad (18)$$

and using FWHM$_{\rm M}$ as the line-width measure,

$$\log \mu_{\rm SE}({\rm H}\beta) = 6.981 + 0.587[\log L({\rm H}\beta_{\rm broad}) - 41.857] + 1.039[\log {\rm FWHM_M}({\rm H}\beta) - 3.599]. \quad (19)$$

The luminosity coefficient b and the line-width coefficient c are roughly as expected from the virial relationship and the R–L relationship, and we note that the line-width coefficient for FWHM$_{\rm M}$ ($c = 1.039$) is much smaller than that of $\sigma_{\rm M}$ ($c = 1.757$), as expected from Figure 3. It is clear that both Equations (18) and (19) overestimate masses at the low end and underestimate them at the high end, thus biasing the prediction. Coefficients based on fits to the relationship between $\log \mu_{\rm SE}$(Hβ) and $\log \mu_{\rm RM}$(Hβ) are given in the top two rows of Table 5, and the fits are shown in panels (a) and (b) of Figure 4. In both cases, the slopes are too shallow. The failure of Equations (18) and (19) to correctly recover $\log \mu_{\rm RM}$(Hβ) suggests that another parameter is required for the single-epoch virial product prediction.

We investigated the possible importance of another parameter by plotting the residuals $\Delta \log \mu = \log \mu_{\rm RM} - \log \mu_{\rm SE}$ against other parameters, specifically luminosity, mass (virial product), Eddington ratio, emission-line lag, and both line width and line-width ratio FWHM$/\sigma_{\rm line}$ for both mean and rms spectra. The most significant correlation between the virial product residuals and other parameters was for Eddington ratio,

Table 2
Radius–Luminosity and Luminosity–Luminosity Relations[a]

Line (1)	x (2)	y (3)	$a \pm \Delta a$ (4)	$b \pm \Delta b$ (5)	x_0 (6)	ε_y (7)	Δ (8)	Figures (9)
1	$\log L_{\rm AGN}$(5100 Å)	$\log \tau$(Hβ)	1.228 ± 0.025	0.482 ± 0.029	43.444	0.213 ± 0.021	0.241	1(a)
2	$\log L$(H$\beta_{\rm broad}$)	$\log \tau$(Hβ)	1.200 ± 0.025	0.492 ± 0.030	41.746	0.218 ± 0.022	0.244	1(b)
3	$\log L$(1350 Å)	$\log \tau$(C IV)	1.915 ± 0.047	0.517 ± 0.036	45.351	0.336 ± 0.041	0.361	7
4	$\log L_{\rm AGN}$(5100 Å)	$\log L$(H$\beta_{\rm broad}$)	41.797 ± 0.017	0.960 ± 0.020	43.444	0.158 ± 0.014	0.171	2
5	$\log L$(H$\beta_{\rm broad}$)	$\log L_{\rm AGN}$(5100 Å)	43.396 ± 0.018	1.003 ± 0.022	41.746	0.161 ± 0.015	0.174	2

Note.
[a] Continuum luminosities, L(5100 Å) and L(1350 Å), and line luminosities, L(Hβ) and L(C IV), are in units of erg s^{-1}. Time delays, τ(Hβ) and τ(C IV), are in days.

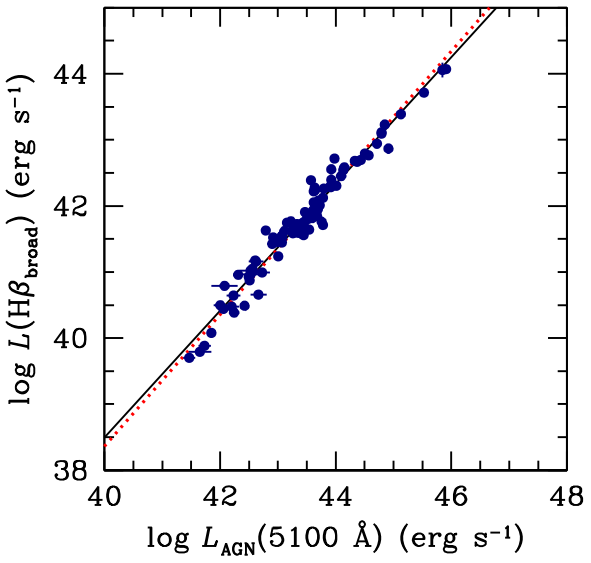

Figure 2. Relationship between the broad Hβ emission line luminosity and the starlight-corrected AGN luminosity for the sources in Table A1. The black solid line is the regression of L(H$\beta_{\rm broad}$) on $L_{\rm AGN}$(5100 Å); the Spearman rank coefficient for this fit is $\rho = 0.901$ with $P < 10^{-6}$. The red dotted line is the regression of $L_{\rm AGN}$(5100 Å) on L(H$\beta_{\rm broad}$), which we use in Equation (24); for this fit $\rho = 0.970$ and $P < 10^{-6}$. The coefficients for both fits are given in Table 2.

which has been a result of other recent investigations (Du et al. 2016, 2018; Grier et al. 2017b; Du & Wang 2019; Fonseca Alvarez et al. 2020; Martínez-Aldama et al. 2019). To determine the Eddington ratio, we start with the Eddington luminosity

$$L_{\rm Edd} = \frac{4\pi G c m_e M}{\sigma_e} = 1.257 \times 10^{38}\left(\frac{M}{M_\odot}\right), \quad (20)$$

where m_e is the electron mass and σ_e is the Thomson cross section. The black hole mass is $\log M = \log f + \log \mu$, and, as explained in the Appendix, we assume $\log f = 0.683 \pm 0.150$ (Batiste et al. 2017), so the Eddington luminosity is

$$\log L_{\rm Edd} = \log f + 38.099 + \log \mu_{\rm RM} = 38.782 + \log \mu_{\rm RM}. \quad (21)$$

The bolometric luminosity can be obtained from the observed 5100 Å AGN luminosity plus a bolometric correction

$$\log L_{\rm bol} = \log L_{\rm AGN}(5100\ \text{Å}) + \log k_{\rm bol}. \quad (22)$$

We ignore inclination effects, and, following Netzer (2019), the bolometric correction we use is

$$\log k_{\rm bol} = 10 - 0.2 \log L_{\rm AGN}(5100\ \text{Å}). \quad (23)$$

Since we are using L(H$\beta_{\rm broad}$) as a proxy for $L_{\rm AGN}$(5100 Å), we substitute L(H$\beta_{\rm broad}$) for $L_{\rm AGN}$(5100 Å) by fitting the luminosities in Table A1, yielding (see Table 2)

$$\log L_{\rm AGN}(5100\ \text{Å}) = 43.396 + 1.003[\log L(\text{H}\beta_{\rm broad}) - 41.746], \quad (24)$$

so we can write the bolometric luminosity as

$$\log L_{\rm bol} = 44.717 + 0.802[\log(\text{H}\beta_{\rm broad}) - 41.746]. \quad (25)$$

The Eddington ratio $\dot{m}$ is given by[23]

$$\log \dot{m} = \log L_{\rm bol} - \log L_{\rm Edd}. \quad (26)$$

Using Equations (25) and (21), the Eddington ratio can then be written as

$$\log \dot{m} = 5.935 + 0.802[\log L(\text{H}\beta_{\rm broad}) - 41.746] - \log \mu_{\rm RM}. \quad (27)$$

To correct the single-epoch masses for Eddington ratio, we fit the equation

$$\Delta \log \mu = \log \mu_{\rm RM} - \log \mu_{\rm SE} = a + b(\log \dot{m} - x_0), \quad (28)$$

and we use this as a correction to our initial fits, Equations (18) and (19). The best-fit parameters for comparison of the $\sigma_{\rm M}$ and FWHM$_{\rm M}$-based predictors of $\mu_{\rm SE}$ with the reverberation measurements $\mu_{\rm RM}$ are given in lines 4 and 5 of Table 5 and shown in panels (a) and (b) of Figure 5. Combining the correction Equation (28) with the best-fit coefficients in Table 5 and Equations (18) and (19) yields the corrected single-epoch masses

$$\log \mu_{\rm SE}(\text{H}\beta) = 6.965 + 0.566[\log L(\text{H}\beta_{\rm broad}) - 41.857] + 1.757[\log \sigma_{\rm M}(\text{H}\beta) - 3.293] - 0.422[\log \dot{m} + 0.951] \quad (29)$$

[23] Strictly speaking, the Eddington ratio is defined as $\dot{m} = \dot{M}/\dot{M}_{\rm Edd}$. Since $\dot{M} = L_{\rm bol}/\eta c^2$, $\dot{m} = L_{\rm bol}/L_{\rm Edd}$ as long as the efficiency η is constant and not a function of the accretion rate, which we will assume for simplicity.

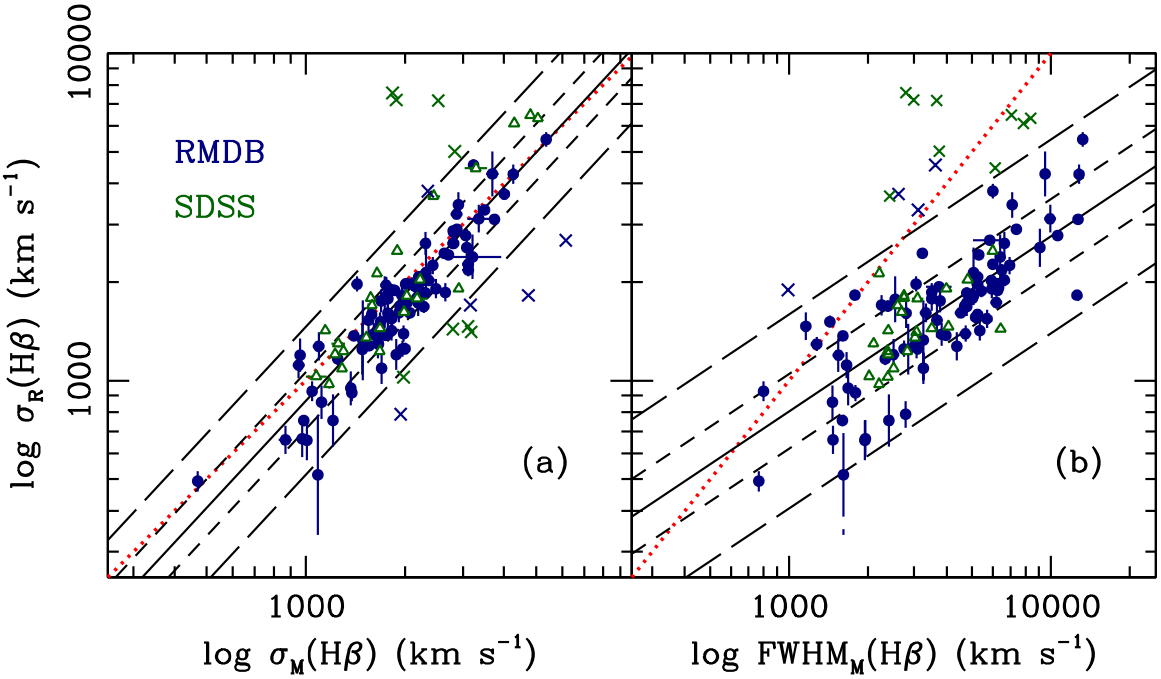

Figure 3. (a) Relationship between Hβ line dispersion in the rms σ_R(Hβ) and mean σ_M(Hβ) spectra. (b) Relationship between Hβ line dispersion in the rms spectrum σ_R(Hβ) and FWHM in the mean spectrum FWHM$_M$(Hβ). Blue filled circles are for the RMDB sample (Table A1), and open green triangles are for the SDSS sample (Table A3). The solid lines are best fits to Equation (10), with coefficients in Table 3. The short- and long-dashed lines indicate the $\pm1\sigma$ and $\pm2.6\sigma$ envelopes, respectively, and the red dotted lines indicate where the two line-width measures are equal. Crosses are points that were rejected at the 2.6σ (99%) level and are colored-coded like the circles. The relationship in panel (a) is nearly linear (slope = 1.085 ± 0.045), and the scatter ε_y is low (0.079 dex). The Spearman rank correlation coefficient for these data is $\rho = 0.901$, and the probability of the correlation arising by chance is $P < 10^{-6}$. It is clear in panel (b) that FWHM$_M$(Hβ) and σ_R(Hβ) are well correlated, but the relationship is significantly nonlinear (slope = 0.535 ± 0.042), the scatter ε_y is slightly larger (0.106 dex), and there are several significant outliers. For these data, $\rho = 0.786$ and $P < 10^{-6}$.

and

$$\log \mu_{\rm SE}({\rm H}\beta) = 6.974 + 0.587[\log L({\rm H}\beta_{\rm broad}) - 41.857] + 1.039[\log {\rm FWHM_M}({\rm H}\beta) - 3.599] - 0.543[\log \dot{m} + 0.951], \quad (30)$$

for σ_M and FWHM$_M$, respectively.

Once the dependence on Eddington ratio is removed (panels (c) and (b) of Figure 4), the residuals do not appear to correlate with other properties. We can now use Equations (29) and (30) to make single-epoch mass predictions, and we plot these versus the reverberation measurements in panels (c) and (d) of Figure 4. The quality of the correction can be tested by fitting these relationships. The best-fit coefficients for the corrected $\log \mu_{\rm SE}$(Hβ)–$\log \mu_{\rm RM}$(Hβ) relationship are given in lines 8 and 9 of Table 5.

4. Masses Based on C IV

4.1. Fundamental Relationships

As noted in Section 1, the veracity of C IV-based mass estimates is unclear and remains controversial. The ideal situation would be to have a large number of AGNs with both C IV and Hβ reverberation measurements to effect a direct comparison. There are, unfortunately, very few AGNs that have both; indeed, Table A2 of the Appendix includes all C IV results for which there are corresponding Hβ measurements in Table A1. For the few sources with both C IV and Hβ reverberation measurements, we plot the virial products $\mu_{\rm RM}$(C IV) and $\mu_{\rm RM}$(Hβ) in Figure 6; these are in each case a weighted mean value of

$$\mu_{\rm RM} = \left(\frac{c\tau\sigma_{\rm R}^2}{G}\right) \quad (31)$$

for each of the observations of Hβ and C IV for the AGNs that appear in both Tables A1 and A2. The close agreement of these values reassures us that the C IV-based RM masses can be trusted, at least over the range of luminosities sampled.

We now need to consider whether or not luminosities and mean line widths are suitable proxies for emission-line lag and rms line widths in the case of C IV. In Figure 7, we show the relationship between the UV continuum luminosity L(1350 Å) and the C IV emission-line lag τ(C IV) based on the C IV data in Table A2, plus the SDSS-RM C IV data in Table A4. The coefficients of the fit are given in line 3 of Table 2. We note again that we have removed from the Grier et al. (2019) sample in Table A4 three quasars with BALs, thus reducing the sample size from 48 to 45. The slope of the C IV R–L relation (0.517) is consistent with that of Hβ (0.492), though the ε_y scatter is substantially greater (0.336 dex for C IV compared to 0.213 dex for Hβ). Definition of the relationship does not depend on the two separate measurements of very short C IV lag measurements for the dwarf Seyfert NGC 4395 (Peterson et al. 2005). Thus, it seems clear that we can use L(1350 Å) as a reasonable proxy for τ(C IV).

We show the relationship between the C IV line dispersion measured in the rms spectrum σ_R(C IV) and the line dispersion in the mean spectrum σ_M(C IV) in Figure 8. The best-fit coefficients are given in line 3 of Table 3. The correlation is good. However, the correlation between FWHM$_M$(C IV) and

Table 3
Line-width Relations[a]

Line (1)	x (2)	y (3)	$a \pm \Delta a$ (4)	$b \pm \Delta b$ (5)	x_0 (6)	ε_y (7)	Δ (8)	Figures (9)
1	$\log \sigma_M(H\beta)$	$\log \sigma_R(H\beta)$	3.260 ± 0.008	1.085 ± 0.045	3.297	0.079 ± 0.006	0.087	3(a)
2	$\log FWHM_M(H\beta)$	$\log \sigma_R(H\beta)$	3.205 ± 0.011	0.535 ± 0.042	3.559	0.106 ± 0.001	0.114	3(b)
3	$\log \sigma_M$(C IV)	$\log \sigma_R$(C IV)	3.436 ± 0.009	0.822 ± 0.059	3.394	0.064 ± 0.008	0.067	8(a)
4	$\log FWHM_M$(C IV)	$\log \sigma_R$(C IV)	3.447 ± 0.016	0.445 ± 0.101	3.580	0.121 ± 0.014	0.121	8(b)

Note.
[a] All line widths are in km s^{-1} in the rest frame of the AGN.

σ_R(C IV), also shown in Figure 8 with coefficients in line 4 of Table 3, is rather poor (see also Wang et al. 2020) and demonstrates that $FWHM_M$(C IV) is a dubious proxy for σ_R(C IV). Measurement of $FWHM_M$(C IV) is clearly a much less reliable predictor of σ_R(C IV) than is σ_M(C IV), so we will not consider $FWHM_M$(C IV) further.

4.2. Single-epoch Masses

Following the same procedures as with Hβ, we use the RMDB data (Table A2) and the SDSS-RM data (Table A4) to fit the equation

$$\log \mu_{RM} = a + b[\log L(1350\ \text{Å}) - x_0] + c[\log \sigma_M(\text{C IV}) - y_0]. \quad (32)$$

The resulting fit is shown in Figure 9, and the best-fit coefficients are given in line 3 of Table 4. Thus, our initial single-epoch virial product prediction is

$$\log \mu_{SE}(\text{C IV}) = 7.664 + 0.599[\log L(1350\ \text{Å}) - 44.706] + 1.014[\log \sigma_M(\text{C IV}) - 3.502]. \quad (33)$$

Single-epoch virial product estimates based on Equation (33) are plotted against the actual reverberation measurements in Figure 9, and the results of a fit to these data are given in line 3 of Table 5. As was the case with Hβ, the slope of this relationship is too shallow, indicating that Equation (33) is too simple a prescription and suggesting that another parameter is required.

Guided by our result for Hβ, we plot the residuals in $\log \mu_{RM} - \log \mu_{SE}$ versus Eddington ratio $\dot{m}$ in panel (a) of Figure 10. The Eddington ratio for the UV data is

$$\log \dot{m} = -33.737 + 0.9 \log L(1350\ \text{Å}) - \log \mu_{RM}, \quad (34)$$

where again we have used a bolometric correction from L (1350 Å) from Netzer (2019),

$$\log k_{bol} = 5.045 - 0.1 \log L(1350\ \text{Å}). \quad (35)$$

We fitted Equation (28) to the C IV mass residuals and Eddington ratio, and the results are given in line 6 of Table 5 and also plotted in panel (a) of Figure 10.

The offset between the residuals in panel (a) of Figure 10 between the RMDB and VP06 data, on one hand, and the SDSS data, on the other hand, might seem to be problematic, and we were initially concerned that this might be a data integrity issue. However, upon examining the distribution of mass and luminosity for these three samples as seen in Figure 11, we see clearly that the mass distribution of the SDSS sources is skewed toward much higher values than for the RMDB and VP06 sources, which are relatively local and less luminous than the SDSS quasars. We will thus proceed by examining mass residuals versus both Eddington ratio and μ_{RM}.

Figure 10 illustrates the process by which we eliminate the mass residuals in successive iterations. We compute the mass residuals $\Delta \log \mu = \log \mu_{RM} - \log \mu_{SE}$ from Equation (33); these are shown versus $\dot{m}$ (left column) and μ_{RM} (right column). We fit these residuals versus $\dot{m}$ (panel (a)) and subtract the best fit to get the corrected residuals shown in the panels (c) and (d). Examination of these residuals as a function of other parameters revealed that they are still correlated with μ_{RM} (panel (d)), suggesting that the importance of the Eddington ratio depends on the black hole mass. We therefore fit the residuals a second time, this time as

$$\Delta \log \mu = a + b(\log \mu_{RM} - x_0). \quad (36)$$

The best fit to this equation is shown in panel (d), and the coefficients are given in Table 5. Subtraction of the best fit yields the residuals shown in panels (e) and (f). We would, under most circumstances, consider this procedure with some trepidation from a statistical point of view, since μ_{RM} appears explicitly in one correction and is implicitly in the Eddington ratio. A generalized solution would have multiple degeneracies, as both mass and luminosity appear in multiple terms. However, the residual corrections are physically motivated; several previous investigations have also concluded that Eddington ratio is correlated with the deviation from the Bentz et al. (2013) R–L relationship, and panels (c) and (d) of Figure 10 suggest that the impact of Eddington ratio varies slightly with mass. Nevertheless, one would prefer to work with parameters that are correlated with or indicators of $\dot{m}$ and μ_{RM}, as we will discuss in Section 6.

Combining the original fit (Equation (33)) with the two corrections (Equations (34) and (36)) yields a corrected single-epoch virial product predictor,

$$\log \mu_{SE}(\text{C IV}) = 7.714 + 0.761[\log L(1350\ \text{Å}) - 44.706] + 1.289[\log \sigma_M(\text{C IV}) - 3.502]. \quad (37)$$

Single-epoch virial products for all three samples are compared with the reverberation measurements in the right panel of Figure 9. The coefficients of the best fit to these data are given in line 10 of Table 5.

It is worth noting in passing that after correcting for Eddington ratio (Figure 5), the residuals in the Hβ-based mass estimates show no correlation with either mass or luminosity.

Table 4
Multivariate Fits[a]

Line	x (erg s^{-1})	y (km s^{-1})	z ($M_\odot$)	$a \pm \Delta a$	$b \pm \Delta b$	$c \pm \Delta c$	x_0 (erg s^{-1})	y_0 (km s^{-1})	ε_z	Δ
(1)	(2)	(3)	(4)	(5)	(6)	(7)	(8)	(9)	(10)	(11)
1	$\log L(\mathrm{H}\beta_{\mathrm{broad}})$	$\log \sigma_{\mathrm{M}}(\mathrm{H}\beta)$	$\log \mu_{\mathrm{RM}}(\mathrm{H}\beta)$	6.975 ± 0.029	0.566 ± 0.035	1.757 ± 0.160	41.857	3.293	0.273 ± 0.025	0.314
2	$\log L(\mathrm{H}\beta_{\mathrm{broad}})$	$\log \mathrm{FWHM}_{\mathrm{M}}(\mathrm{H}\beta)$	$\log \mu_{\mathrm{RM}}(\mathrm{H}\beta)$	6.981 ± 0.033	0.587 ± 0.040	1.039 ± 0.128	41.857	3.559	0.323 ± 0.028	0.352
3	$\log L(1350\ \text{Å})$	$\log \sigma_{\mathrm{M}}(\mathrm{C\ IV})$	$\log \mu_{\mathrm{RM}}(\mathrm{C\ IV})$	7.664 ± 0.039	0.599 ± 0.033	1.014 ± 0.265	44.706	3.502	0.364 ± 0.033	0.397

Note.
[a] All values of μ_{RM} are in solar masses.

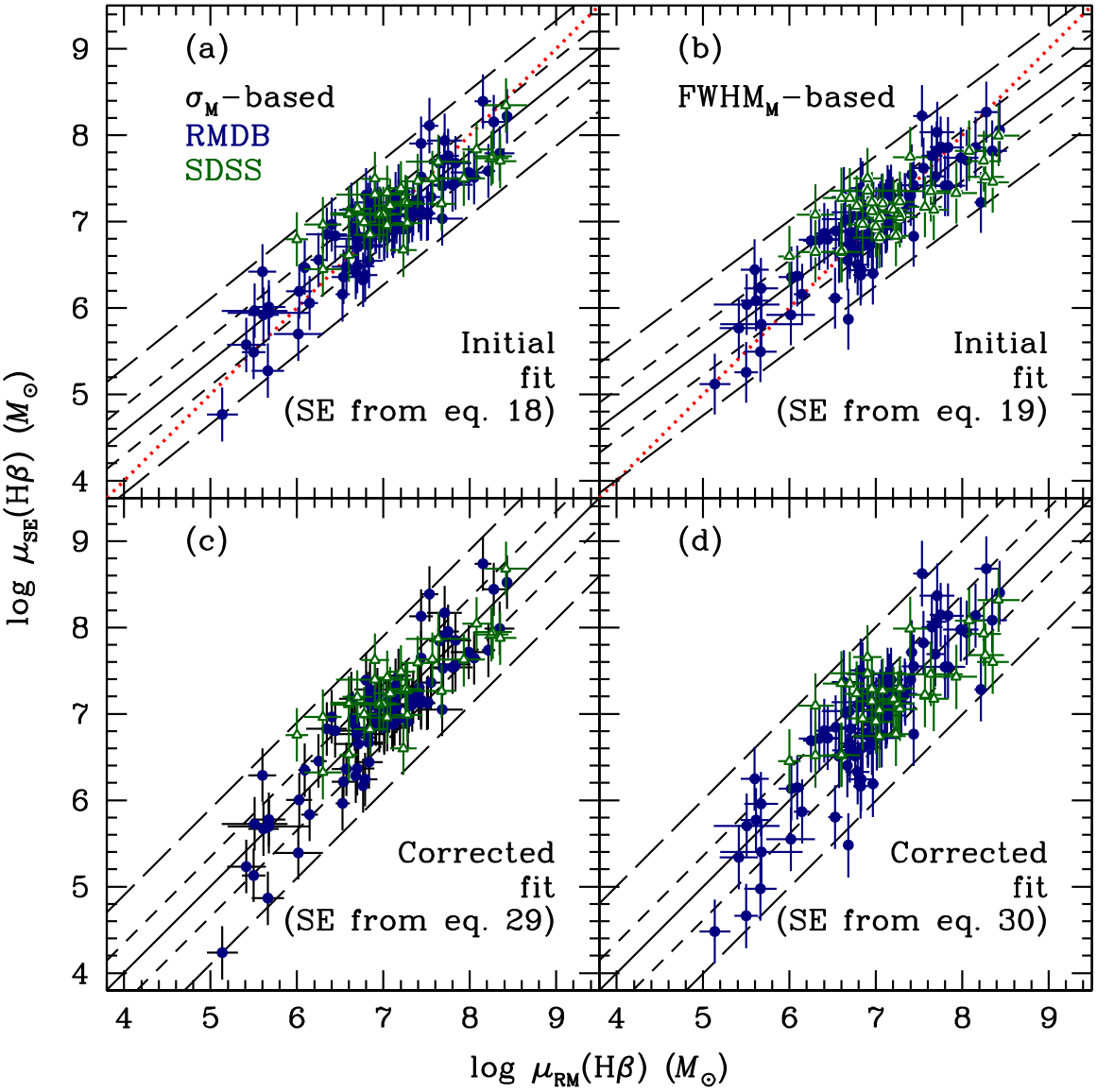

Figure 4. Single-epoch Hβ-based virial product predictions using Equations (18) and (19) in panels (a) and (b), respectively, compared with the actual RM measurements for the same sources. The coefficients and their uncertainties for these initial predictors of $\log \mu_{SE}(H\beta)$ are presented in the first two lines of Table 4. Blue filled circles represent RMDB data (Table A1), and green open triangles represent SDSS data (Table A3). The solid line shows the best fit to the data, and the red dotted line shows where the two values are equal. Coefficients for fits to the $\log \mu_{SE}(H\beta)$–$\log \mu_{RM}(H\beta)$ relationship are given in the first two lines of Table 5. The short- and long-dashed lines show the $\pm 1\sigma$ and $\pm 2.6\sigma$ envelopes, respectively. It is clear that this is an inadequate virial product predictor, as it systematically underestimates higher masses and overestimates lower masses. Panels (c) and (d) show the same relationship after the empirical corrections as embodied in Equations (29) and (30) for σ_M and FWHM$_M$, respectively. In panels (c) and (d), the best-fit lines cover the equality lines; results of these fits are given in lines 8 and 9 of Table 5. The intrinsic errors ε_y have been added in quadrature to the measurement uncertainties in $\log \mu_{SE}(H\beta)$.

5. Computing Single-epoch Masses

To briefly reiterate our approach so far, we started with the assumption that $\mu_{SE} = f(R, L)$ only. This proved to be inadequate, so we examined the residuals in the $\log \mu_{SE}$–$\log \mu_{RM}$ relationship and found that these correlated best with Eddington ratio $\dot{m}$: fundamentally, at increasing $\dot{m}$, the Bentz et al. (2013) *R–L* relationship overpredicts the size of the BLR *R* (Du & Wang 2019). In the case of C IV, we found additional residuals that correlated with μ_{RM}, although we cannot definitively demonstrate that some part of this is not attributable to inhomogeneities in the database (a point that will be pursued in the future). While we believe that this analysis identifies the physical parameters that affect the mass estimates, there are multiple degeneracies, with both mass and luminosity appearing in more than one term.

Instead of trying to fit coefficients to all the physical parameters that have been identified, we can do a purely empirical correction to Equations (16), (17), and (32) since the residuals in the $\log \mu_{RM}$–$\log \mu_{SE}$ relationships (top panels of Figure 4 and left panel of Figure 9) are rather small. We can combine the basic *R–L* fits (Equations (16), (17), and (32)) with the residual fits (Equations (28) and (36)) to obtain prescriptions that work over the mass range sampled. Renormalizing for convenience, we can estimate single-epoch masses based on H$\beta(\sigma_M)$ from

$$\log M_{SE} = \log f + 7.530 + 0.703[\log L(H\beta) - 42] + 2.183[\log \sigma_M(H\beta) - 3.5], \quad (38)$$

Table 5
Initial, Residual, and Final Fits

Line (1)	Data Set (2)	x (3)	y (4)	$a \pm \Delta a$ (5)	$b \pm \Delta b$ (6)	x_0 (7)	ε_y (8)	Δ (9)	Figures (10)
	Initial:								
1	Hβ	$\log \mu_{\rm RM}(\sigma_{\rm M})$	$\log \mu_{\rm SE}(\sigma_{\rm M})$	7.025 ± 0.025	0.805 ± 0.038	7.041	0.249 ± 0.021	0.279	4(a)
2	Hβ	$\log \mu_{\rm RM}({\rm FWHM_M})$	$\log \mu_{\rm SE}({\rm FWHM_M})$	7.012 ± 0.028	0.749 ± 0.042	7.007	0.278 ± 0.023	0.290	4(b)
3	C IV	$\log \mu_{\rm RM}$(C IV)	$\log \mu_{\rm SE}$(C IV)	7.483 ± 0.033	0.787 ± 0.041	7.481	0.321 ± 0.028	0.347	9(a)
	Residual:								
4	Hβ	$\log \dot{m}$	$\Delta \log \mu(\sigma_{\rm M})$	-0.010 ± 0.022	-0.422 ± 0.045	−0.951	0.187 ± 0.021	0.246	5(a)
5	Hβ	$\log \dot{m}$	$\Delta \log \mu({\rm FWHM_M})$	-0.007 ± 0.023	-0.543 ± 0.046	−0.951	0.191 ± 0.021	0.247	5(b)
6	C IV	$\log \dot{m}$	$\Delta \log \mu$	-0.049 ± 0.026	-0.557 ± 0.048	−1.155	0.213 ± 0.027	0.282	10(a)
7	C IV	$\log \mu_{\rm RM}$	$\Delta \log \mu$	-0.012 ± 0.026	0.297 ± 0.024	7.481	0.000 ± 0.000	0.139	10(d)
	Final:								
8	Hβ	$\log \mu_{\rm RM}(\sigma_{\rm M})$	$\log \mu_{\rm SE}(\sigma_{\rm M})$	7.040 ± 0.031	0.999 ± 0.047	7.041	0.309 ± 0.027	0.346	4(c)
9	Hβ	$\log \mu_{\rm RM}({\rm FWHM_M})$	$\log \mu_{\rm SE}({\rm FWHM_M})$	7.007 ± 0.037	1.000 ± 0.055	7.007	0.371 ± 0.030	0.387	4(d)
10	C IV	$\log \mu_{\rm RM}$(C IV)	$\log \mu_{\rm SE}$(C IV)	7.485 ± 0.041	0.963 ± 0.006	7.481	0.408 ± 0.035	0.439	9(b)

with associated uncertainty

$$\Delta \log M_{\rm SE} = \{(\Delta \log f)^2 + [0.703\ \Delta \log L({\rm H}\beta)]^2 + [2.183\ \Delta \log \sigma_{\rm M}({\rm H}\beta)]^2\ \}^{1/2}. \quad (39)$$

Here f is the scaling factor, which is discussed briefly in the Appendix, and $\Delta \log P$ is the uncertainty in the parameter $\log P$. The intrinsic scatter in this relationship is 0.309 dex, and this must be added in quadrature to the random error. For the case of Hβ(FWHM$_{\rm M}$), a single-epoch mass estimate is obtained from

$$\log M_{\rm SE} = \log f + 7.015 + 0.784[\log L({\rm H}\beta) - 42] + 1.387[\log {\rm FWHM_M}({\rm H}\beta) - 3.5], \quad (40)$$

with associated uncertainty

$$\Delta \log M_{\rm SE} = \{(\Delta \log f)^2 + [0.784\ \Delta \log L({\rm H}\beta)]^2 + [1.387\ \Delta \log {\rm FWHM_M}({\rm H}\beta)]^2\ \}^{1/2}. \quad (41)$$

In this case, the intrinsic scatter is 0.371 dex.

A comparison of the reverberation-based virial products $\mu_{\rm RM}$(Hβ) and the single-epoch masses $\mu_{\rm SE}$(Hβ) based on Equations (38) and (40) is shown in panels (c) and (d) of Figure 4.

Similarly, single-epoch masses based on C IV can be computed from

$$\log M_{\rm SE} = \log f + 7.934 + 0.761[\log L(1350\ {\rm \AA}) - 45] + 1.289[\log \sigma_{\rm M}({\rm C\ IV}) - 3.5], \quad (42)$$

with associated uncertainty

$$\Delta \log M_{\rm SE} = \{(\Delta \log f)^2 + [0.761\ \Delta \log L(1350\ {\rm \AA}]^2 + [1.289\ \Delta \log \sigma_{\rm M}({\rm C\ IV})]^2\ \}^{1/2}. \quad (43)$$

The intrinsic scatter in this relationship is 0.408 dex. Single-epoch predictions and reverberation-based masses for the AGNs in Tables A2, A4, and A5 are compared in panel (b) of Figure 9. Coefficients for this fit are given in line 10 of Table 5.

In Figure 12, we show the distribution in bolometric luminosity and black hole mass based on our prescriptions for the entire sample of SDSS-RM quasars for which Hβ or C IV single-epoch masses can be estimated.

6. Discussion

6.1. Single-epoch Masses

Our primary goal has been to find simple, yet unbiased, prescriptions for estimating the masses of the black holes that power AGNs. Our underlying assumption has been that the most accurate measure of the virial product is given by using the emission-line lag τ and line width in the rms spectrum $\sigma_{\rm R}$ (e.g., Equation (A1) in the Appendix), as that quantity produces, upon adjusting by the scaling factor f, an $M_{\rm BH}$–σ_* relationship for AGNs that is in good agreement with that for quiescent galaxies. Given that both τ and $\sigma_{\rm R}$ average over structure in a complex system (see Barth et al. 2015), it is somewhat surprising that this method of mass estimation works as well as it does.

Here we have shown that the luminosity of the broad component of the Hβ emission line is a good proxy for the starlight-corrected AGN luminosity (Figure 1). This is useful since it eliminates the difficult task of accurately modeling the host-galaxy starlight contribution to the continuum luminosity. Moreover, the line luminosity and $\sigma_{\rm R}$ reflect the BLR state at the same time; a measurement of the continuum luminosity, by contrast, better represents the state of the BLR at a time τ in the future on account of the light-travel time delay within the system (Pogge & Peterson 1992; Gilbert & Peterson 2003; Barth et al. 2015); this is, however, generally a very small effect. For the sake of completeness, we also note that there is a small, but detectable, lag between continuum variations at shorter wavelengths and those at longer wavelengths (McHardy et al. 2014, 2018; Shappee et al. 2014; Edelson et al. 2015, 2017, 2019; Fausnaugh et al. 2016).

We have also confirmed that, for the case of Hβ, both $\sigma_{\rm M}$ and FWHM$_{\rm M}$ are reasonable proxies for $\sigma_{\rm R}$, though $\sigma_{\rm M}$ is somewhat better than FWHM$_{\rm M}$.

On the other hand, the case of C IV remains problematic, as it differs in a number of ways from the other strong emission lines:

1. The equivalent width (EW) of C IV decreases with luminosity, which is known as the Baldwin effect (Baldwin 1977); C IV is driven by higher-energy photons than, say, the Balmer lines, and the Baldwin effect reflects a softening of the high-ionization continuum. This could be due to higher Eddington ratio (Baskin &

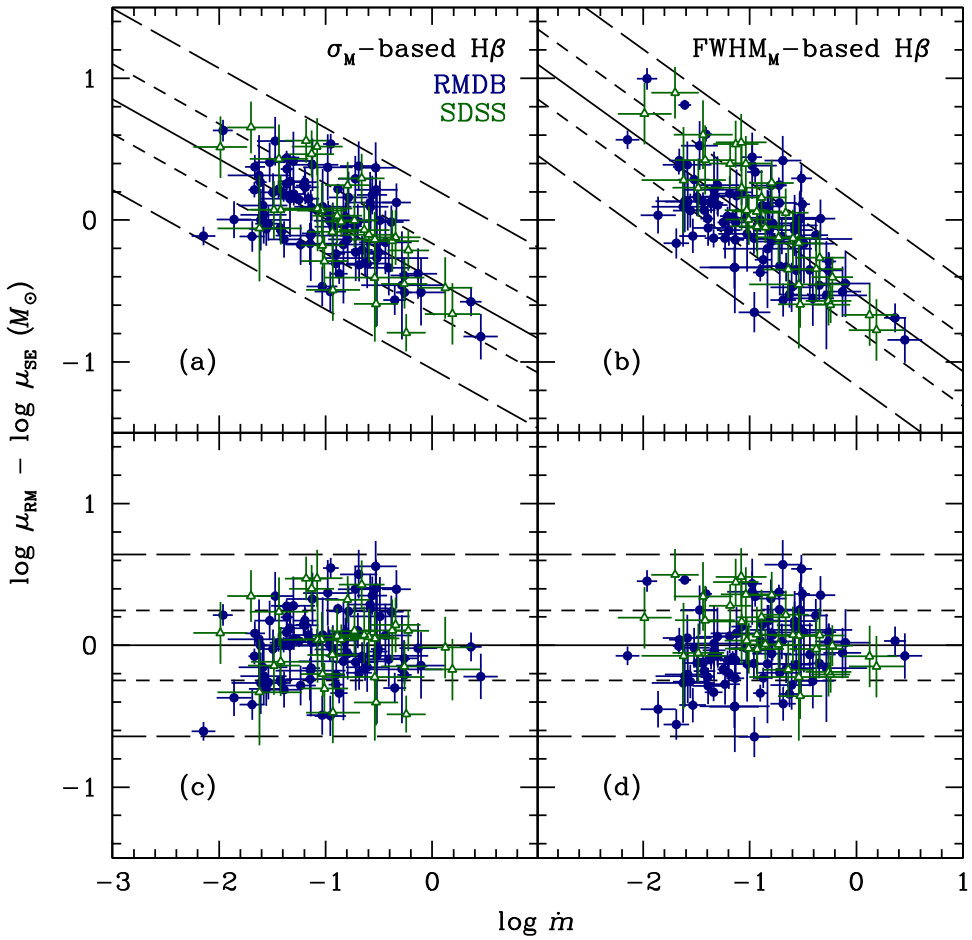

Figure 5. (a) Mass residuals (Equation (28)) are the difference between the measured reverberation virial products and those predicted by Equation (18). The residuals are plotted vs. Eddington ratio $\dot{m}$ (Equation (27)) for single-epoch virial products based on σ_M(Hβ). The Spearman rank correlation coefficient is $\rho = -0.577$, with the probability that the correlation arises by chance $P < 10^{-6}$. (b) Mass residuals (Equation (28)) are the difference between the measured reverberation virial products and those predicted by Equation (19). The residuals are plotted vs. Eddington ratio $\dot{m}$ for single-epoch virial products based on FWHM$_M$(Hβ). For these data, $\rho = -0.679$ with $P < 10^{-6}$. Panels (c) and (d) show residuals after subtraction of the best fit in panels (a) and (b), respectively. The ε_y scatter in the residuals is 0.197 dex for the σ_M-based virial products and 0.204 dex for the FWHM$_M$-based virial products. In all panels, the filled blue circles represent RMDB data (Table A1) and the open green triangles represent SDSS data (Table A3). The solid line shows the best fit to the data. The short- and long-dashed lines are the $\pm 1\sigma$ and $\pm 2.6\sigma$ envelopes, respectively. The coefficients of the fits are given in Table 5. Error bars on the residuals are measurement uncertainties only, without systematic errors.

Laor 2004) or because more massive black holes have cooler accretion disks (Korista et al. 1998).

2. The C IV emission line is typically blueshifted with respect to the systemic redshift of the quasar, which is attributed to outflow of the BLR gas (Gaskell 1982; Wilkes 1984, 1986; Espey et al. 1989; Corbin 1990; Wills et al. 1993; Richards et al. 2002, 2011; Sulentic et al. 2007; Coatman et al. 2016; Shen 2016; Bisogni et al. 2017; Vietri et al. 2018).
3. BALs in the short-wavelength wing of C IV, another signature of outflow, are common (Weymann et al. 1991; Hall et al. 2002; Hewett & Foltz 2003; Allen et al. 2011). We remind the reader that in Section 2.1 we removed ∼17% of our SDSS C IV sample because the presence of BALs precludes accurate line-width measurements.
4. The pattern of "breathing" in C IV is the opposite of what is seen in Hβ (Wang et al. 2020). Breathing refers to the response of the emission lines, both lag and line width, to changes in the continuum luminosity. In the case of Hβ, an increase in luminosity produces an increase in lag and a decrease in line width (Gilbert & Peterson 2003; Goad et al. 2004; Cackett & Horne 2006). In the case of C IV, however, the line width increases when the continuum luminosity increases, contrary to expectations from the virial theorem (Equation (2)).

We must certainly be mindful that outflows can affect a mass measurement, though the effect is small if the gas is at escape velocity. Notably, in the cases studied to date there is good agreement between Hβ-based and C IV-based virial products (Figure 7), though, again, these are local Seyfert galaxies that are not representative of the general quasar population.

The C IV breathing issue is addressed in detail by Wang et al. (2020), building on evidence for a nonreverberating narrow core or blue excess in the C IV emission line presented by Denney (2012). In this two-component model, the variable part of the line is much broader than the nonvariable core. As the continuum brightens, the variable broad component increases in prominence, resulting in a larger value of σ_M. As the broad component reverberates in response to continuum variations, σ_M will track σ_R much better than FWHM$_M$, thus explaining the breathing characteristics and why FWHM$_M$ is a poor line-width measure for estimating black hole masses. Physical interpretation of the nonvarying core remains an open question;

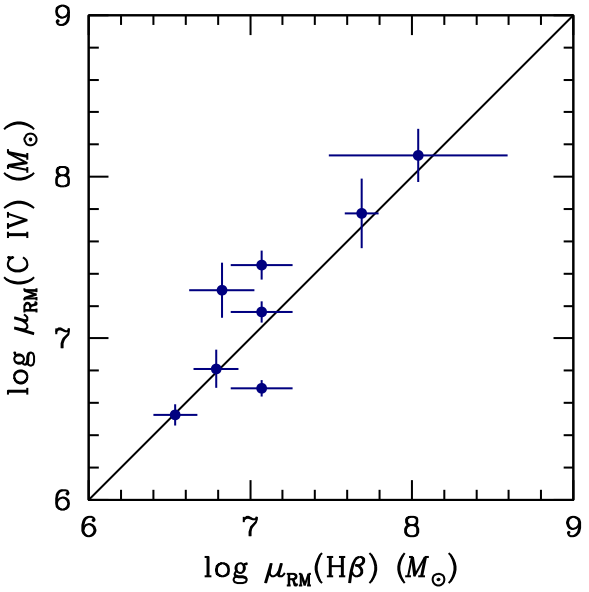

Figure 6. Virial products based on C IV and Hβ for the few cases in the RMDB sample for which both are available. The solid line is the locus where the two virial products are equal. The values are weighted means of μ_{RM}(Hβ) and μ_{RM}(C IV) for individual AGNs that appear in both Tables A1 and A2. The Spearman rank coefficient for these data is $\rho = 0.805$, and the probability that the correlation arises by chance is $P = 0.016$.

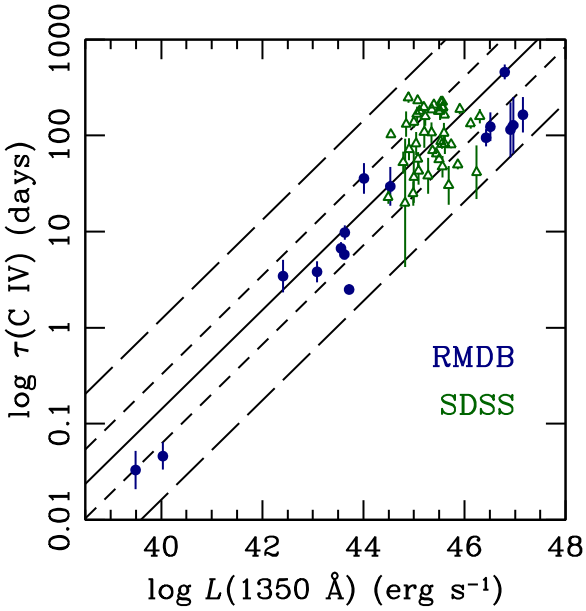

Figure 7. Relationship between the C IV rest-frame emission-line lag τ(C IV) and the continuum luminosity at 1350 Å. Blue filled circles represent RMDB data (Table A2), and green open triangles represent SDSS data (Table A4). The solid line is the best fit to the data using Equation (10), with coefficients given in Table 2. The short- and long-dashed lines are the $\pm 1\sigma$ and $\pm 2.6\sigma$ envelopes, respectively. The Spearman rank coefficient for these data is $\rho = 0.503$, with a probability $P = 1.1 \times 10^{-5}$ that the correlation arises by chance. If the two lowest-luminosity points (both measurements of the dwarf Seyfert NGC 4395) are omitted, the Spearman rank coefficient is decreased to $\rho = 0.481$ with $P = 1.1 \times 10^{-4}$.

Denney (2012) suggests that it might be an optically thin disk wind or an inner extension of the narrow-line region.

6.2. Eigenvector 1 and the Role of Eddington Ratio

Aside from the Baldwin effect (Baldwin 1977), the average spectra of quasars show little dependence on luminosity (e.g., Vanden Berk et al. 2004). However, individual objects show considerable spectral diversity or differences from the mean spectrum, regardless of luminosity. Many of these spectral differences show strong correlations and anticorrelations with other spectral properties or physical parameters as revealed by principal component analysis (PCA), as first shown by Boroson & Green (1992). The strongest of these multiple correlations, Eigenvector 1, is most clearly characterized by the anticorrelation between (a) the strength of the Fe II λ4570 and Fe II $\lambda\lambda$5190, 5320 complexes on either side of the broad Hβ complex and (b) the strength of the [O III] $\lambda\lambda$4959, 5007 doublet. The Fe II strength is typically characterized by the ratio of the EW or fluxes of Fe II to Hβ, i.e., $\mathcal{R}$(Fe II) = EW(Fe II)/EW(Hβ). Boroson & Green (1992) speculate that the physical driver behind Eigenvector 1 is Eddington ratio, as they are able to argue against inclination effects. Sulentic et al. (2000) incorporated UV data into the PCA and found that the magnitude of the C IV emission-line blueshift, a ubiquitous feature of AGN UV spectra (e.g., Richards et al. 2002), is also an Eigenvector 1 component, with larger blueshifts associated with higher $\mathcal{R}$(Fe II) and lower [O III] strength. This has been confirmed in a number of subsequent studies (Baskin & Laor 2005; Coatman et al. 2016; Sulentic et al. 2017). Sulentic et al. (2000) also demonstrated that the "narrow-line Seyfert 1" (NLS1) galaxies (Osterbrock & Pogge 1985), a subset of type 1 AGNs with particularly small broad-line widths (FWHM(Hβ) < 2000 km s^{-1}), lie at the strong $\mathcal{R}$(Fe II)–weak [O III] extreme of Eigenvector 1. To see why this is so, if we combine the R–L relation with Equation (2), the expected line-width dependence is seen to be

$$V \propto \left(\frac{M}{L^{1/2}}\right)^{1/2} \propto \left(\frac{M}{\dot{m}}\right)^{1/4}, \tag{44}$$

where $\dot{m} \propto L/M$ is the Eddington ratio (Equation (26)). Thus, AGNs with the highest Eddington ratios have the smallest broad-line widths, and many such sources are classified as NLS1s. Boroson (2002) argues that the physical parameter driving Eigenvector 1 is indeed Eddington ratio and that Eigenvector 2 is driven by accretion rate; these two physical parameters, plus inclination, appear to account for most of the spectral diversity among quasars. There is now, we believe, general consensus in the literature that Eigenvector 1 is driven by Eddington ratio (e.g., Shen & Ho 2014; Sun & Shen 2015; Marziani et al. 2018), and our own analysis supports this.

The necessity of including an Eddington ratio correction to single-epoch mass estimators became an issue when poor agreement was found between Hβ- and Mg II-based single-epoch masses, on one hand, and C IV-based masses, on the other. Shen et al. (2008b) found that the offset between Mg II-based single-epoch masses and those based on C IV correlated with the C IV blueshift, an Eigenvector 1 parameter as already noted, thus enabling an empirical correction. Similarly, Runnoe et al. (2013a) and Brotherton et al. (2015a) use the strength of the Si IV–O IV] blend, another Eigenvector 1 parameter, to effect an empirical correction.

The Super-Eddington Accreting Massive Black Holes (SEAMBH) collaboration has focused on high-$\dot{m}$ candidates in their RM program (Du et al. 2014, 2016, 2018; Du & Wang 2019). An important result from these studies, as we have noted earlier, is that the Hβ lags are smaller than

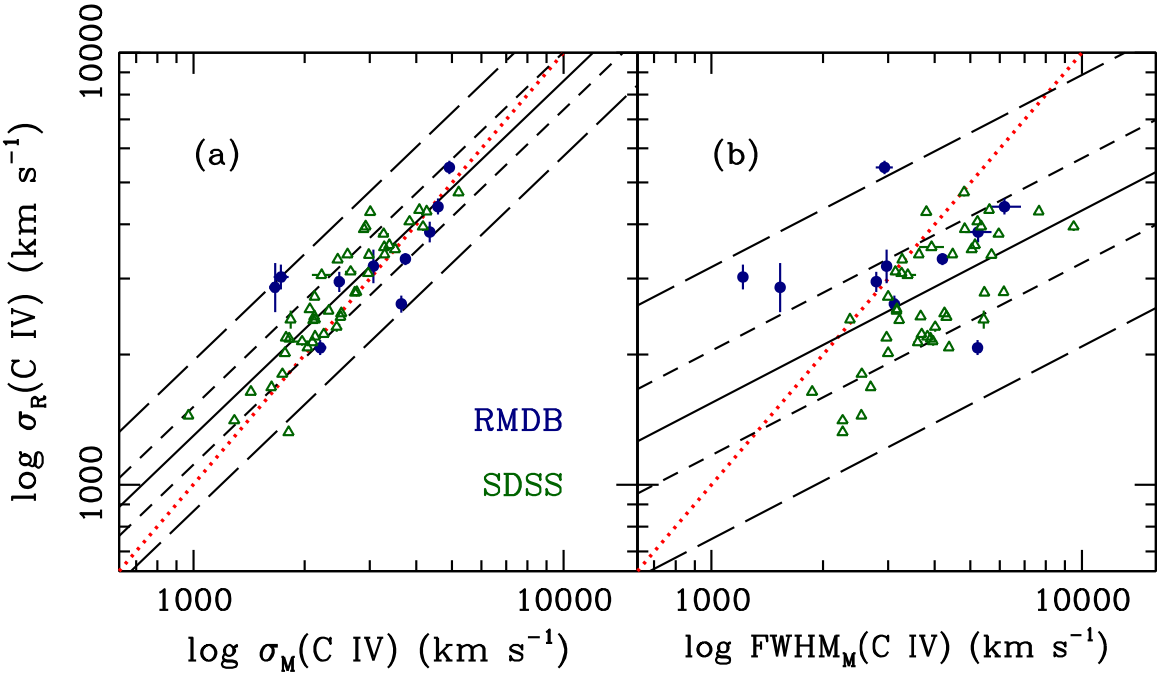

Figure 8. (a) Relationship between C IV line dispersion in the mean and rms spectra of reverberation-mapped AGNs. The Spearman rank coefficient is $\rho = 0.873$, with a probability of $P < 10^{-6}$ that the correlation arises by chance. (b) Relationship between $\mathrm{FWHM_M}$(C IV) and σ_{R}(C IV) for reverberation-mapped AGNs. The Spearman rank coefficient for these data is $\rho = 0.524$ with $P = 3.96 \times 10^{-5}$. In both panels, blue filled circles represent RMDB sources in Table A2 and green open triangles represent SDSS-RM sources in Table A4. The red dotted line shows the locus where the two line-width measures are equal. The solid line is the best fit to Equation (10), and the coefficients are given in Table 3. The short- and long-dashed lines show the $\pm 1\sigma$ and $\pm 2.6\sigma$ envelopes, respectively.

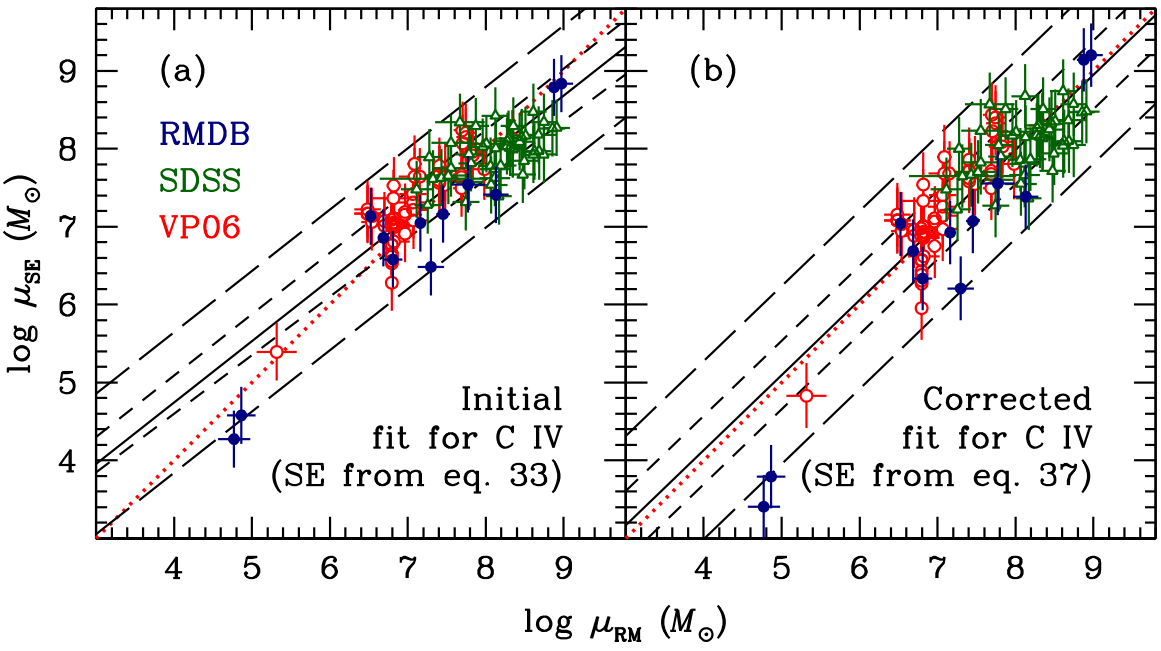

Figure 9. (a) Comparison of single-epoch virial products μ_{SE}(C IV) and reverberation measurements μ_{RM}(C IV) for the data in Table A2 (blue filled circles), the SDSS-RM C IV reverberation data from Table A4 (green open triangles), and data from Table A5 (red open circles). The solid line is the best fit to the data and has slope 0.787 ± 0.041. As was the case with Hβ, masses are overestimated at the low end and underestimated at the high end, with the exception of the three very low mass measurements. (b) Comparison of single-epoch virial products after empirical correction as given in Equation (42). In both panels, the solid line is the best fit to the relationship between $\log \mu_{\mathrm{SE}}$(C IV) and $\log \mu_{\mathrm{RM}}$(C IV). The short- and long-dashed lines define the $\pm 1\sigma$ and $\pm 2.6\sigma$ envelopes, respectively. The diagonal red dotted line is the locus where μ_{RM} and μ_{SE} are equal. Coefficients for both fits are given in Table 5, in line 3 for panel (a) and in line 10 for panel (b). In both panels, the intrinsic errors ε_y have been added in quadrature to the measurement errors in $\log \mu_{\mathrm{SE}}$(C IV).

predicted by the current state-of-the-art *R–L* relationship (Bentz et al. 2013). This implies that in these objects the ratio of hydrogen-ionizing photons to optical photons is lower than in the lower-$\dot{m}$ sources; this is also consistent with the relative strength of $\mathcal{R}$(Fe II), the weakness of high-ionization lines such as [O III], and the soft X-ray spectra (Boller et al. 1996) of

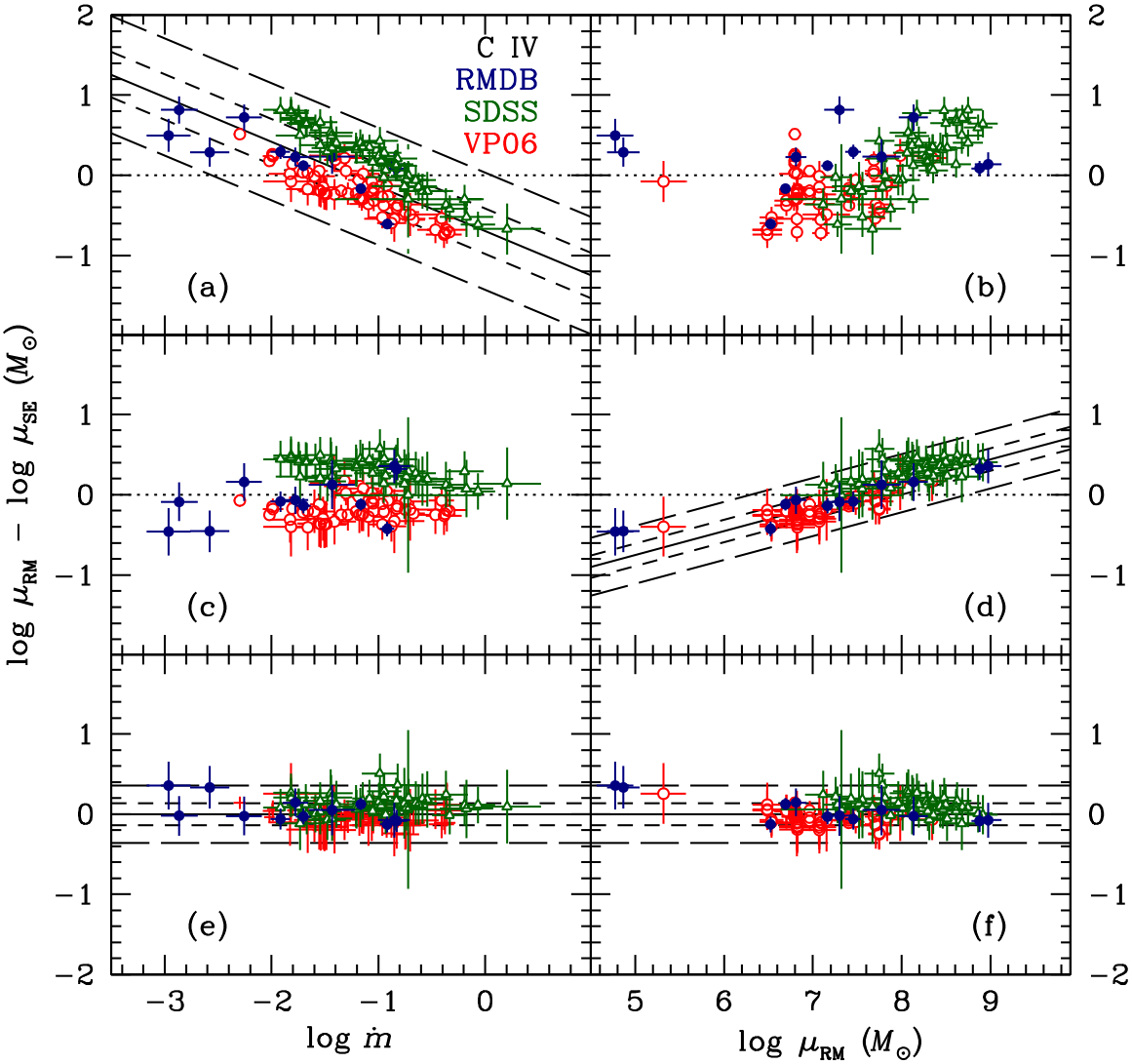

Figure 10. Mass residuals $\Delta \log \mu = \log \mu_{\rm RM} - \log \mu_{\rm SE}$ vs. Eddington rate $\dot{m}$ (left column) and virial product $\mu_{\rm RM}$ (right column) for C IV. Panel (a) shows the residuals between $\mu_{\rm RM}$(C IV) and $\mu_{\rm SE}$(C IV) vs. Eddington ratio $\dot{m}$ (Equation (26)). The fit to these data has Spearman rank coefficient $\rho = -0.693$, with a probability that the correlation arises by chance $P < 10^{-6}$. Panel (b) shows the residuals vs. virial product $\mu_{\rm RM}$. Panels (c) and (d) show the residuals vs. $\dot{m}$ and $\mu_{\rm RM}$ after subtracting the fit in panel (a). Panel (d) also shows a best fit to the residuals vs. mass; coefficients are given in line 7 of Table 5. Note that there is no intrinsic scatter in this relationship because the error bars are so large. For these data, $\rho = 0.883$ and $P < 10^{-6}$. Panels (e) and (f) show the mass residuals vs. $\dot{m}$ and $\mu_{\rm RM}$ after subtracting the fit in panel (d). The scatter in panels (e) and (f) is 0.138 dex. In all panels, the blue filled circles represent RMDB data (Table A2), the green open triangles are SDSS data (Table A4), and the red open circles are VP06 data (Table A5). Best fits are shown as solid lines, and the short- and long-dashed lines indicate the $\pm 1\sigma$ and $\pm 2.6\sigma$ envelopes, respectively.

high-$\dot{m}$ sources. Du & Wang (2019) choose to make their correction to the BLR radius through adding a term that correlates with the deficiency of ionizing photons. In our approach, we absorb the correction directly into the virial product computation.

The studies cited above have noted that an Eddington ratio correction is required for single-epoch masses based on Hβ. We find, as have others (Shen et al. 2008b; Bian et al. 2012; Shen & Liu 2012; Runnoe et al. 2013a; Brotherton et al. 2015a; Coatman et al. 2017), that a similar correction is required for C IV-based masses as well.

As noted in Section 4.2, from a statistical point of view, in the single-epoch mass equations it would be preferable to replace the Eddington ratio with a parameter strongly correlated with it. However, we find that the scatter in these relationships is so large that any gain in the accuracy of black hole mass estimates is offset by a large loss of precision. For example, while the correlation between $\mathcal{R}$(Fe II) and Eddington ratio exists, as shown for the SDSS-RM sample in Figure 13, the scatter is so large that the correlation has no real predictive power. We therefore elect at this time to focus on the empirical formulae given in Section 5.

6.3. Future Improvements

While we believe that our current single-epoch prescription for estimating quasar black hole masses is more accurate than previous prescriptions, we also recognize that there are additional improvements that can be made to improve both accuracy and precision, some of which we became aware of near the end of the current project. We intend to implement these in the future. Topics that we will investigate in the future include the following:

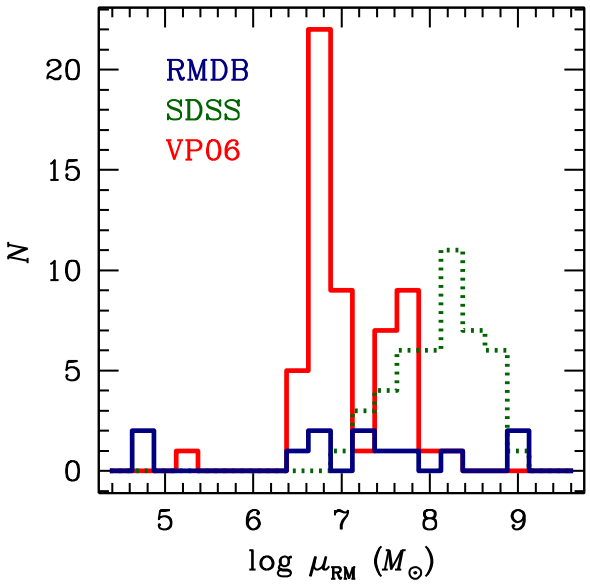

Figure 11. Distribution in virial product $\mu_{\rm RM}$ for the RMDB (Table A2; blue solid line), SDSS (Table A3; green dotted line), and VP06 (Table A4; red solid line) samples. The VP06 sample is a subset of the RMDB sample, which is dominated by the relatively low mass Seyfert galaxies that were the first sources studied by RM. The SDSS quasars are comparatively more massive and more luminous.

1. Replace those reverberation lag measurements made with the interpolated cross-correlation function (Gaskell & Peterson 1987; White & Peterson 1994; Peterson et al. 1998b, 2004) with lag measurements and uncertainties from JAVELIN (Zu et al. 2011). Recent tests (Li et al. 2019; Yu et al. 2020) show that while the JAVELIN and interpolation cross-correlation lags are generally consistent, the uncertainties predicted by JAVELIN are more reliable.
2. Utilize the expanded SDSS-RM database, which now extends over 6 yr, not only to make use of additional lag detections but also to capitalize on the gains in S/N that will increase the overall quality of the lag and line-width measurements and result in fewer rejections of poor data.
3. Expand the database in Table A1 with recent results and other previous results that we excluded because they did not have starlight-corrected continuum luminosities.
4. Update the VP06 database used to produce Table A5. There are now additional reverberation-mapped AGNs with archived HST UV spectra. Some of the poorer data in Table A5 can be replaced by measurements based on higher-quality spectra.
5. Consider use of other line-width measures that may correlate well with $\sigma_{\rm line}$ but are less sensitive to blending in the wings. Mean absolute deviation (MAD) is one such candidate; indeed, Park et al. (2017) have already demonstrated that C IV-based masses are more consistent with those based on other lines if either $\sigma_{\rm line}$ or MAD is used instead of FWHM to characterize the line width.
6. Improve line-width measurements. There appear to be some systematic differences among the various data sets, probably due to different processes for measuring $\sigma_{\rm M}$; for example, panels (e) and (f) of Figure 10 show that the single-epoch mass estimates for the VP06 sample are slightly higher than those from SDSS (compare also the last two columns in Table A5). Work on deblending algorithms would aid more precise measurement of $\sigma_{\rm M}$, in particular.

7. Summary

The main results of this paper are as follows:

1. We confirm that the luminosity of the broad component of the Hβ emission line $L({\rm H}\beta_{\rm broad})$ is an excellent substitute for the AGN continuum luminosity $L_{\rm AGN}(5100\,\text{Å})$ for predicting the Hβ emission-line reverberation lag $\tau({\rm H}\beta)$. It has the advantage of being easier to isolate than $L_{\rm AGN}(5100\,\text{Å})$, which requires an accurate estimate of the host-galaxy starlight contribution to the observed luminosity. The fact that there is no statistical penalty for using $L({\rm H}\beta)$ as the luminosity measure is, from a practical point of view, one of the most important findings of this work because the high-quality unsaturated space-based images that are used for host-galaxy modeling (see Bentz et al. 2013, and references therein) may not be so easily acquired in the future.
2. We confirm that the line dispersion of the Hβ broad component $\sigma_{\rm M}({\rm H}\beta)$ and the FWHM for the Hβ broad component ${\rm FWHM_M}({\rm H}\beta)$ in mean, or single-epoch, spectra are both reasonable proxies for the line dispersion of Hβ in the rms spectrum $\sigma_{\rm M}({\rm H}\beta)$ for computing single-epoch virial products $\mu_{\rm SE}({\rm H}\beta)$. We find that $\sigma_{\rm M}({\rm H}\beta)$ gives better results than ${\rm FWHM_M}({\rm H}\beta)$, but both are usable.
3. In the case of C IV, we find that the line dispersion of the C IV emission line $\sigma_{\rm M}$(C IV) in the mean, or single-epoch, spectrum is a good proxy for the line dispersion in the rms spectrum $\sigma_{\rm R}$(C IV) for estimating single-epoch virial products $\mu_{\rm SE}$(C IV). We find that ${\rm FWHM_M}$(C IV), however, does not track $\sigma_{\rm R}$(C IV) well enough to be used as a proxy.
4. Although the R–L relationship based on the continuum luminosity $L(1350\,\text{Å})$ and C IV emission-line reverberation lag τ(C IV) is not as well defined as that for Hβ, the relationship appears to have a similar slope, and it appears to be suitable for estimating virial products $\mu_{\rm SE}$(C IV).
5. We confirm for both Hβ and C IV that combining the reverberation lag estimated from the luminosity with a suitable measurement of the emission-line width together introduces a bias where the high masses are underestimated and the low masses are overestimated. We confirm that the parameter that accounts for the systematic difference between reverberation virial product measurements $\mu_{\rm RM}$ and those estimated using only luminosity and line width is Eddington ratio. Increasing Eddington ratio causes the reverberation radius to shrink, suggesting a softening of the hydrogen-ionizing spectrum.
6. While the virial product estimate from combining luminosity and line width causes a systematic bias, the relationship between the reverberation virial product $\mu_{\rm RM}$ and the single-epoch estimate $\mu_{\rm SE}$ is still a power law, but with a slope somewhat less than unity (top panels of Figure 4, left panel of Figure 9). We are therefore able to empirically correct this relationship to an unbiased estimator of $\mu_{\rm SE}$ by fitting the residuals and essentially rotating the power-law distribution to have a slope of

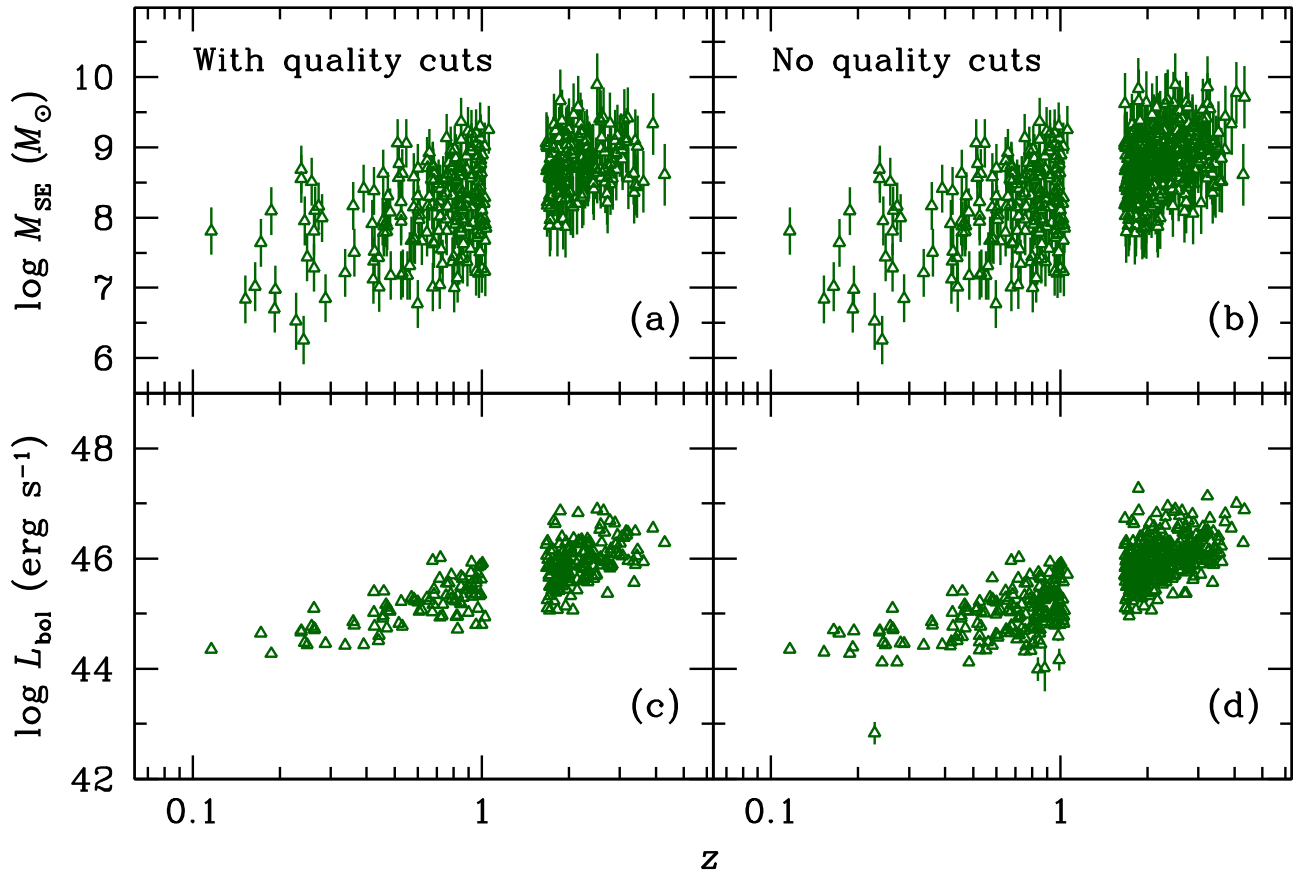

Figure 12. Distribution of masses (panels (a) and (b)) and bolometric luminosities (panels (c) and (d)) for the entire SDSS-RM sample for which Hβ or C IV single-epoch masses can be computed using Equations (38) and (42). Here we assume $f = 4.28$ (Batiste et al. 2017). Bolometric corrections were made using Equations (23) and (35). In the left column, the quality cuts of Section 2.1 have been imposed. In the right column, no quality cuts have been made.

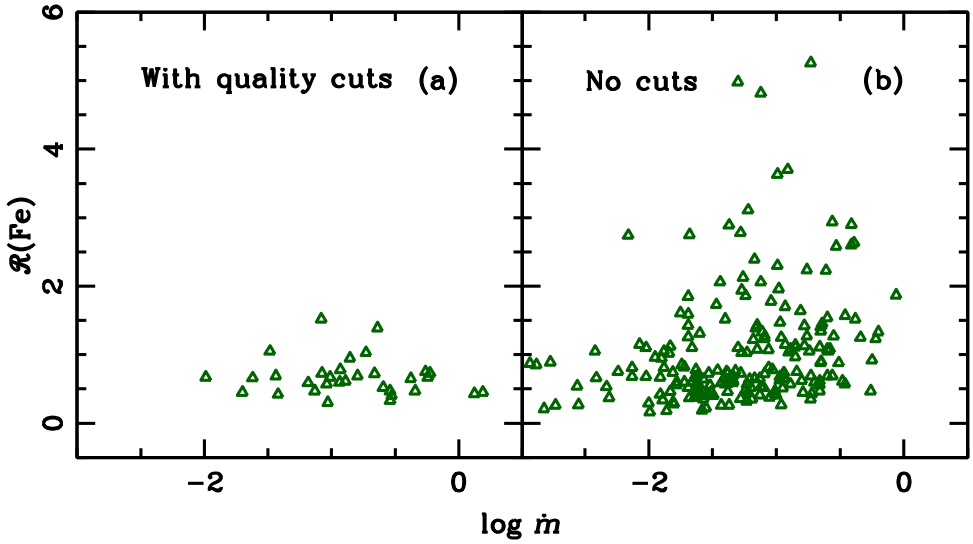

Figure 13. Correlation between $\mathcal{R}$(Fe) and Eddington ratio $\dot{m}$ for the subset of SDSS-RM quasars selected for our study on the basis of quality cuts (Section 2.1) in panel (a) and for all SDSS-RM quasars with measured Fe II EWs in the compilation of Shen et al. (2019) in panel (b). The Eddington ratio used by Shen et al. (2019) differs slightly from that used here.

unity (bottom panels of Figure 4, right panel of Figure 9). We present these empirical estimators for μ_{SE}(Hβ) and μ_{SE}(C IV) in Section 5. On account of its potential utility, we regard this as the most important conclusion of this study.

The authors are grateful to the referee for suggestions that improved the presentation. E.D.B. is supported by Padua University through grants DOR1715817/17, DOR1885254/18, and DOR1935272/19 and by MIUR grant PRIN 2017 20173ML3WW_001. E.D.B. and B.M.P. are grateful for the

hospitality of STScI early in this investigation. J.V.H.S. and K.H. acknowledge support from STFC grant ST/R000824/1. Y.S. acknowledges support from an Alfred P. Sloan Research Fellowship and NSF grant AST-1715579. C.J.G., W.N.B., J.R.T., and D.P.S. acknowledge support from NSF grants AST-1517113 and AST-1516784. K.H. acknowledges support from STFC grant ST/R000824/1. P.B.H. acknowledges support from NSERC grant 2017-05983. Y.H. acknowledges support from NASA through STScI grant HST-GO-15650. S.W., L.J., and L.C.H. acknowledge support from the National Science Foundation of China (11721303, 11890693, 11991052) and the National Key R&D Program of China (2016YFA0400702, 2016YFA0400703). M.V. gratefully acknowledges support from the Independent Research Fund Denmark via grant No. DFF 8021-00130.

Funding for the Sloan Digital Sky Survey IV has been provided by the Alfred P. Sloan Foundation, the U.S. Department of Energy Office of Science, and the Participating Institutions. SDSS-IV acknowledges support and resources from the Center for High-Performance Computing at the University of Utah. The SDSS website is www.sdss.org. SDSS-IV is managed by the Astrophysical Research Consortium for the Participating Institutions of the SDSS Collaboration, including the Brazilian Participation Group, the Carnegie Institution for Science, Carnegie Mellon University, the Chilean Participation Group, the French Participation Group, Harvard-Smithsonian Center for Astrophysics, Instituto de Astrofísica de Canarias, Johns Hopkins University, Kavli Institute for the Physics and Mathematics of the Universe (IPMU)/University of Tokyo, the Korean Participation Group, Lawrence Berkeley National Laboratory, Leibniz Institut für Astrophysik Potsdam (AIP), Max-Planck-Institut für Astronomie (MPIA Heidelberg), Max-Planck-Institut für Astrophysik (MPA Garching), Max-Planck-Institut für Extraterrestrische Physik (MPE), National Astronomical Observatories of China, New Mexico State University, New York University, University of Notre Dame, Observatário Nacional/MCTI, The Ohio State University, Pennsylvania State University, Shanghai Astronomical Observatory, United Kingdom Participation Group, Universidad Nacional Autónoma de México, University of Arizona, University of Colorado Boulder, University of Oxford, University of Portsmouth, University of Utah, University of Virginia, University of Washington, University of Wisconsin, Vanderbilt University, and Yale University.

Appendix
Database of Reverberation-mapped AGNs

Reverberation-mapped AGNs provide the fundamental data that anchor the AGN mass scale. We selected all AGNs from the literature (as of 2019 August) for which unsaturated host-galaxy images acquired with HST are available, since removal of the host-galaxy starlight contribution to the observed luminosity is critical to this calibration and measurements of Hβ time lags. It is worth noting, however, that since our analysis shows that the broad Hβ flux is a useful proxy for the 5100 Å continuum luminosity, this criterion is overrestrictive, and we will avoid imposing it in future compilations. In many cases, there is more than one RM data set available in the literature. In a few cases, the more recent data were acquired to replace, say, a more poorly sampled data set or one for which the initial result was ambiguous for some reason. In other cases, there are multiple data sets of comparable quality for individual AGNs, and in these cases we include them all. The particularly well-studied AGN NGC 5548 has been observed many times and in some sense has served as a "control" source that provides our best information about the repeatability of mass measurements, as the continuum and line widths show long-term (compared to reverberation timescales) variations.

The final reverberation-mapped sample for Hβ is given in Table A1. It consists of 98 individual time series for 50 individual low-redshift ($z < 0.3$) AGNs. They span a range of AGN luminosity $41.46 \leqslant \log L(5100\ \text{Å}) \leqslant 45.81$, in erg s^{-1}. Luminosities have been corrected for Galactic absorption using extinction values on the NASA Extragalactic Database, which are based on the Schlafly & Finkbeiner (2011) recalibration of the Schlegel et al. (1998) dust map. Line-width and time-delay measurements are in the rest frame of the AGNs. Luminosity distances are based on redshift, except the cases noted by Bentz et al. (2013), for which the redshift-independent distances quoted in that paper are used. For two of these sources, NGC 4051 and NGC 4151, we use preliminary Cepheid-based distances (M. M. Fausnaugh 2020, private communication), and for NGC 6814, we use the Cepheid-based distance from Bentz et al. (2019). Individual virial products for these sources are easily computed using the Hβ time lags (Column (6)) and line dispersion measurements (Column (12)) and the formula

$$\mu = 0.1952\left(\frac{\tau(\mathrm{H}\beta)}{\text{days}}\right)\left(\frac{\sigma_{\mathrm{R}}(\mathrm{H}\beta)}{\text{km s}^{-1}}\right)^2 M_{\odot}. \quad \text{(A1)}$$

Further conversion to mass requires multiplication by the virial factor f, i.e., $\log M = \log f + \log \mu$, a dimensionless factor that depends on the inclination, structure, and kinematics of the broad-Hβ-emitting region—indeed, detailed modeling of nine of these objects (Pancoast et al. 2014; Grier et al. 2017a) shows that f depends most clearly on inclination (Grier et al. 2017a). Since such models are available for only a very limited number of AGNs, it is more common to use a statistical estimate of a mean value of f based on a secondary mass indicator, specifically the well-known M_{BH}–σ_* relationship (Ferrarese & Merritt 2000; Gebhardt et al. 2000; Gültekin et al. 2009), where σ_* is the host-galaxy stellar bulge velocity dispersion. The required assumption is that the AGN M_{BH}–σ_* is identical to that of quiescent galaxies (Woo et al. 2013). In fact, it is found that the μ–σ_* has a slope consistent with the M_{BH}–σ_* slope for quiescent galaxies (Grier et al. 2013), and the zero-points disagree by only a multiplicative factor, which is taken to be f. Here we take $\langle \log f \rangle = 0.683 \pm 0.150$ (Batiste et al. 2017), where the error on the mean is $\Delta \log f = 0.030$—this error must be propagated into the mass measurement error when comparing AGN reverberation-based masses to those based on other methods. In Table A2, we list all published C IV reverberation measurements that we regard as reliable. In Tables A3 and A4, we list all published SDSS-RM measurements that meet our selection criteria for Hβ and C IV, respectively. Finally, in Table A5 we present single-epoch C IV-based mass estimates from VP06 as described in Section 2.1.

Table A1
Reverberation-mapped AGNs (Hβ)

Source	References	JD Range (−2,400,000)	z	D_L (Mpc)	τ(Hβ) (days)	log $L_{\rm total}$(5100) (erg s^{-1})	log $L_{\rm AGN}$(5100) (erg s^{-1})	log L(H$\beta_{\rm broad}$) (erg s^{-1})	FWHM$_{\rm M}$(Hβ) (km s^{-1})	$\sigma_{\rm M}$(Hβ) (km s^{-1})	$\sigma_{\rm R}$(Hβ) (km s^{-1})
(1)	(2)	(3)	(4)	(5)	(6)	(7)	(8)	(9)	(10)	(11)	(12)
Mrk 335	1	49156–49338	0.02579	109.5	$16.8^{+4.8}_{-4.2}$	43.802 ± 0.010	43.703 ± 0.013	42.083 ± 0.010	1792 ± 3	1380 ± 6	917 ± 52
Mrk 335	1	49889–50118	0.02579	109.5	$12.5^{+6.6}_{-5.5}$	43.861 ± 0.010	43.777 ± 0.013	42.124 ± 0.010	1679 ± 2	1371 ± 8	948 ± 113
Mrk 335	1	55431–55569	0.02579	109.5	$14.3^{+0.7}_{-0.7}$	43.791 ± 0.007	43.683 ± 0.061	41.940 ± 0.009	1273 ± 3	1663 ± 6	1293 ± 64
Mrk 1501	2	55430–55568	0.08934	402.5	$12.6^{+3.9}_{-3.9}$	44.314 ± 0.011	43.980 ± 0.053	42.719 ± 0.015	3106 ± 15	3494 ± 35	3321 ± 107
PG 0026+129	3	48545–51084	0.14200	653.1	$111.0^{+24.1}_{-28.3}$	44.977 ± 0.010	44.911 ± 0.011	42.867 ± 0.016	2544 ± 56	1738 ± 100	1773 ± 285
PG 0052+251	3	48461–51084	0.15445	751.9	$89.8^{+24.5}_{-24.1}$	44.964 ± 0.013	44.791 ± 0.020	43.113 ± 0.016	5008 ± 73	2167 ± 30	1783 ± 86
Fairall 9	4	49475–49743	0.04702	202.8	$17.4^{+3.2}_{-4.3}$	44.224 ± 0.007	43.920 ± 0.026	42.393 ± 0.007	5999 ± 60	2347 ± 16	3787 ± 197
Mrk 590	1	48090–48323	0.02639	112.1	$20.7^{+3.5}_{-2.7}$	43.842 ± 0.010	43.544 ± 0.029	41.855 ± 0.011	2788 ± 29	1942 ± 26	789 ± 74
Mrk 590	1	48848–49048	0.02639	112.1	$14.0^{+8.5}_{-8.8}$	43.666 ± 0.011	43.075 ± 0.073	41.522 ± 0.011	3729 ± 426	2168 ± 30	1935 ± 52
Mrk 590	1	49183–49338	0.02639	112.1	$29.2^{+4.9}_{-5.0}$	43.743 ± 0.010	43.320 ± 0.043	41.690 ± 0.010	2743 ± 79	1967 ± 19	1251 ± 72
Mrk 590	1	49958–50122	0.02639	112.1	$28.8^{+3.6}_{-4.2}$	43.865 ± 0.010	43.589 ± 0.026	41.857 ± 0.010	2500 ± 43	1880 ± 19	1201 ± 130
3C 120	1	47837–50388	0.03301	140.9		44.078 ± 0.012	44.010 ± 0.014	42.306 ± 0.012	2327 ± 48	1249 ± 21	1166 ± 50
3C 120	5	54726–54920	0.03301	140.9	$27.9^{+7.1}_{-5.9}$	44.116 ± 0.013	44.094 ± 0.013	42.453 ± 0.012	2386 ± 52	⋯	1689 ± 68
3C 120	2	55430–55569	0.03301	140.9	$25.9^{+2.3}_{-2.3}$	43.993 ± 0.012	43.903 ± 0.052	42.298 ± 0.015	1430 ± 16	1687 ± 4	1514 ± 65
Ark 120	1	48148–48344	0.03271	139.6	$47.1^{+8.3}_{-12.4}$	44.254 ± 0.010	43.921 ± 0.032	42.553 ± 0.010	6042 ± 35	1753 ± 6	1959 ± 109
Ark 120	1	49980–50175	0.03271	139.6	$37.1^{+4.8}_{-5.4}$	44.131 ± 0.010	43.569 ± 0.067	42.390 ± 0.010	6246 ± 78	1862 ± 13	1884 ± 48
MCG +08-11-011	6	56639–56797	0.02048	86.6	$15.72^{+0.50}_{-0.52}$	43.574 ± 0.009	43.282 ± 0.045	41.706 ± 0.006	1159 ± 8	1681 ± 2	1466 ± 143
Mrk 6	7	49250–49872	0.01881	80.6	$21.2^{+4.}_{-3.2}$	43.576 ± 0.009	43.351 ± 0.033	41.591 ± 0.011	⋯	2813 ± 13	2836 ± 48
Mrk 6	7	49980–50777	0.01881	80.6	$20.7^{+3.0}_{-2.4}$	43.578 ± 0.009	43.354 ± 0.033	41.632 ± 0.010	⋯	2804 ± 6	2626 ± 37
Mrk 6	7	50869–51516	0.01881	80.6	$20.5^{+5.6}_{-7.0}$	43.523 ± 0.011	43.258 ± 0.042	41.584 ± 0.013	⋯	2808 ± 14	2626 ± 37
Mrk 6	7	51557–53356	0.01881	80.6	$23.9^{+17.0}_{-7.3}$	43.431 ± 0.007	43.070 ± 0.058	41.449 ± 0.018	⋯	2870 ± 13	3222 ± 39
Mrk 6	7	53611–54804	0.01881	80.6	$20.4^{+4.6}_{-4.1}$	43.613 ± 0.005	43.413 ± 0.027	41.579 ± 0.012	⋯	2807 ± 8	2864 ± 35
Mrk 6	2	55340–55569	0.01881	80.6	$10.1^{+1.1}_{-1.1}$	43.719 ± 0.008	43.507 ± 0.029	41.849 ± 0.012	2619 ± 24	4006 ± 6	3714 ± 68
Mrk 79	1	47838–48044	0.02219	94.0	$9.0^{+8.3}_{-7.8}$	43.668 ± 0.011	43.569 ± 0.014	41.818 ± 0.011	5056 ± 85	2314 ± 23	2137 ± 375
Mrk 79	1	48193–48393	0.02219	94.0	$16.1^{+6.6}_{-6.6}$	43.754 ± 0.010	43.675 ± 0.012	41.851 ± 0.010	4760 ± 31	2281 ± 26	1683 ± 72
Mrk 79	1	48905–49135	0.02219	94.0	$16.0^{+6.4}_{-5.8}$	43.695 ± 0.010	43.602 ± 0.013	41.820 ± 0.010	4766 ± 71	2312 ± 21	1854 ± 72
Mrk 374	6	56663–56795	0.04263	183.3	$14.84^{+5.76}_{-3.30}$	43.994 ± 0.009	43.752 ± 0.036	41.764 ± 0.013	3250 ± 19	1490 ± 4	1329 ± 373
PG 0804+761	3	48319–51085	0.10000	447.5	$146.9^{+18.8}_{-18.9}$	44.905 ± 0.011	44.849 ± 0.011	43.230 ± 0.012	3053 ± 38	1434 ± 18	1971 ± 105
NGC 2617	6	56639–56797	0.01421	59.8	$4.32^{+1.1}_{-1.35}$	43.099 ± 0.011	42.610 ± 0.096	41.173 ± 0.012	5303 ± 48	2709 ± 6	2424 ± 89
Mrk 704	8	55932–55980	0.02923	124.5	$12.65^{+1.49}_{-2.14}$	43.708 ± 0.005	43.517 ± 0.025	41.800 ± 0.007	3502 ± 31	2650 ± 4	1860 ± 120
Mrk 110	1	48953–49149	0.03529	150.9	$24.3^{+5.5}_{-8.3}$	43.711 ± 0.011	43.618 ± 0.014	42.055 ± 0.011	1543 ± 5	962 ± 15	1196 ± 141
Mrk 110	1	49751–49874	0.03529	150.9	$20.4^{+10.5}_{-6.3}$	43.771 ± 0.010	43.691 ± 0.012	41.960 ± 0.010	1658 ± 3	953 ± 10	1115 ± 103
Mrk 110	1	50010–50262	0.03529	150.9	$33.3^{+14.9}_{-10.0}$	43.594 ± 0.012	43.468 ± 0.017	41.905 ± 0.012	1600 ± 39	987 ± 18	755 ± 29
Mrk 110	9	51495–51678	0.03529	150.9	$23.4^{+3.6}_{-3.2}$	43.340 ± 0.007	43.225 ± 0.011	41.769 ± 0.007	⋯	⋯	⋯
PG 0953+414	3	48319–50997	0.23410	1137.2	$150.1^{+21.6}_{-22.6}$	45.193 ± .010	45.126 ± 0.011	43.390 ± 0.012	3071 ± 27	1659 ± 31	1306 ± 144
NGC 3227	10	54184–54269	0.00386	23.7	$3.75^{+0.76}_{-0.82}$	42.629 ± 0.035	42.243 ± 0.068	40.387 ± 0.035	3972 ± 25	1749 ± 4	1376 ± 44
NGC 3227	8	55933–56048	0.00386	23.7	$1.29^{+1.56}_{-1.27}$	42.757 ± 0.006	42.424 ± 0.051	40.487 ± 0.010	1602 ± 2	1402 ± 2	1368 ± 38
Mrk 142	11	54506–54618	0.04494	193.5	$2.74^{+0.73}_{-0.83}$	43.709 ± 0.010	43.543 ± 0.015	41.639 ± 0.010	1462 ± 2	1116 ± 22	859 ± 102
Mrk 142	12	56237–56413	0.04494	193.5	$6.4^{+0.8}_{-2.2}$	43.610 ± 0.010	43.443 ± 0.016	41.586 ± 0.010	1647 ± 69	⋯	⋯
NGC 3516	14,15	54181–54300	0.00884	37.1	$11.68^{+1.02}_{-1.53}$	43.299 ± 0.055	42.726 ± 0.133	40.995 ± 0.057	5236 ± 12	1584 ± 1	1591 ± 10
NGC 3516	8	55932–56072	0.00884	37.1	$5.74^{+2.26}_{-2.04}$	43.272 ± 0.007	42.529 ± 0.196	41.022 ± 0.008	3231 ± 14	2633 ± 3	2448 ± 69
SBS 1116+583A	11	54550–54618	0.02787	118.5	$2.31^{+0.62}_{-0.49}$	42.995 ± 0.021	42.076 ± 0.224	40.788 ± 0.015	3668 ± 186	1552 ± 36	1528 ± 184

Table A1
(Continued)

Source	References	JD Range (−2,400,000)	z	D_L (Mpc)	$\tau(\mathrm{H}\beta)$ (days)	$\log L_{\mathrm{total}}(5100)$ (erg s^{-1})	$\log L_{\mathrm{AGN}}(5100)$ (erg s^{-1})	$\log L(\mathrm{H}\beta_{\mathrm{broad}})$ (erg s^{-1})	$\mathrm{FWHM_M}(\mathrm{H}\beta)$ (km s^{-1})	$\sigma_{\mathrm{M}}(\mathrm{H}\beta)$ (km s^{-1})	$\sigma_{\mathrm{R}}(\mathrm{H}\beta)$ (km s^{-1})
(1)	(2)	(3)	(4)	(5)	(6)	(7)	(8)	(9)	(10)	(11)	(12)
Arp 151	11,13	54506–54618	0.02109	89.2	$3.99^{+0.49}_{-0.68}$	42.979 ± 0.010	42.497 ± 0.047	40.931 ± 0.011	3098 ± 69	2006 ± 24	1252 ± 46
NGC 3783	14,15	48607–48833	0.00973	25.1	$10.2^{+3.3}_{-2.3}$	42.791 ± 0.025	42.559 ± 0.051	41.009 ± 0.021	3770 ± 68	1691 ± 19	1753 ± 141
Mrk 1310	11	54550–54618	0.01956	82.7	$3.66^{+0.59}_{-0.61}$	42.937 ± 0.018	42.231 ± 0.120	40.646 ± 0.012	2409 ± 24	1209 ± 42	755 ± 138
NGC 4051	16	54180–54311	0.00234	15.0	$1.87^{+0.54}_{-0.50}$	42.290 ± 0.015	41.847 ± 0.080	40.079 ± 0.018	799 ± 2	1045 ± 4	927 ± 64
NGC 4051	6	56645–56864	0.00234	15.0	$2.87^{+0.86}_{-1.33}$	42.265 ± 0.005	41.732 ± 0.106	39.882 ± 0.012	765 ± 3	470 ± 2	493 ± 35
NGC 4151	17	53430–53472	0.00332	15.0	$6.59^{+1.12}_{-0.76}$	42.549 ± 0.012	42.004 ± 0.113	40.499 ± 0.013	5840 ± 863	6158 ± 47	2680 ± 64
NGC 4151	6	55931–56072	0.00332	15.0	$6.82^{+0.48}_{-0.57}$	42.685 ± 0.007	42.315 ± 0.060	40.956 ± 0.008	992 ± 4	1833 ± 2	1894 ± 9
Mrk 202	11	54550–54617	0.02102	88.9	$3.05^{+1.73}_{-1.12}$	42.946 ± 0.016	42.198 ± 0.126	40.477 ± 0.010	1471 ± 18	867 ± 40	659 ± 65
NGC 4253	11	54509–54618	0.01293	54.4	$6.16^{+1.63}_{-1.22}$	42.948 ± 0.012	42.509 ± 0.044	40.873 ± 0.010	1609 ± 39	1088 ± 37	⋯
PG 1226+023	3	48361–50997	0.15834	737.7	$306.80^{+68.5}_{-90.9}$	45.935 ± 0.011	45.907 ± 0.011	44.072 ± 0.014	3509 ± 36	1778 ± 17	1777 ± 150
3C 273	18	54795–58194	0.15834	737.7	$146.3^{+8.3}_{-12.1}$	45.864 ± 0.011	45.848 ± 0.011	44.056 ± 0.010	3256 ± 36	1701 ± 15	1090 ± 121
PG 1229+204	3	48319–50997	0.06301	274.9	$37.8^{+27.6}_{-15.3}$	44.053 ± 0.010	43.636 ± 0.040	42.275 ± 0.011	3828 ± 54	1608 ± 24	1385 ± 111
NGC 4593	19	53391–53580	0.00900	37.7	$3.73^{+0.75}_{-0.75}$	43.242 ± 0.013	43.005 ± 0.035	41.237 ± 0.013	5143 ± 16	1790 ± 3	1561 ± 55
NGC 4748	11	54550–54618	0.01463	61.6	$5.55^{+1.62}_{-2.22}$	43.072 ± 0.012	42.557 ± 0.060	41.047 ± 0.010	1947 ± 66	1009 ± 27	657 ± 91
PG 1307+085	3	48319–51042	0.15500	718.7	$105.6^{+36.0}_{-46.6}$	44.849 ± 0.012	44.790 ± 0.013	43.096 ± 0.020	5059 ± 133	1963 ± 47	1820 ± 122
MCG –06-30-15	20	55988–56079	0.00775	25.5	$5.33^{+1.86}_{-1.75}$	42.393 ± 0.009	41.651 ± 0.197	39.793 ± 0.011	1958 ± 75	976 ± 8	665 ± 87
NGC 5273	21	56774–56838	0.00362	15.3	$2.21^{+1.19}_{-1.60}$	42.000 ± 0.009	41.465 ± 0.106	39.702 ± 0.010	5688 ± 163	1821 ± 53	1544 ± 98
Mrk 279	22	50095–50289	0.03045	129.7	$16.7^{+3.9}_{-3.9}$	43.882 ± 0.021	43.643 ± 0.036	42.242 ± 0.021	5354 ± 32	1823 ± 11	1420 ± 96
PG 1411+442	3	48319–51038	0.08960	398.2	$124.3^{+61.0}_{-61.7}$	44.603 ± 0.012	44.502 ± 0.014	42.792 ± 0.014	2801 ± 43	1774 ± 29	1607 ± 169
NGC 5548	23,24,25	47509–47809	0.01718	72.5	$19.7^{+1.5}_{-1.5}$	43.534 ± 0.021	43.328 ± 0.042	41.728 ± 0.018	4674 ± 63	1934 ± 5	1687 ± 56
NGC 5548	24,25	47861–48179	0.01718	72.5	$18.6^{+2.1}_{-2.3}$	43.390 ± 0.029	43.066 ± 0.068	41.546 ± 0.029	5418 ± 107	2227 ± 20	1882 ± 83
NGC 5548	24,26	48225–48534	0.01718	72.5	$15.9^{+2.9}_{-2.5}$	43.496 ± 0.017	43.264 ± 0.042	41.645 ± 0.026	5236 ± 87	2205 ± 16	2075 ± 81
NGC 5548	24,26	48623–48898	0.01718	72.5	$11.0^{+1.9}_{-2.0}$	43.360 ± 0.020	42.999 ± 0.070	41.457 ± 0.030	5986 ± 95	3110 ± 53	2264 ± 88
NGC 5548	24,27	48954–49255	0.01718	72.5	$13.0^{+1.6}_{-1.4}$	43.497 ± 0.016	43.267 ± 0.040	41.691 ± 0.016	5930 ± 42	2486 ± 13	1909 ± 129
NGC 5548	24,28	49309–49636	0.01718	72.5	$13.4^{+3.8}_{-4.3}$	43.509 ± 0.022	43.287 ± 0.043	41.649 ± 0.022	7378 ± 39	2877 ± 17	2895 ± 114
NGC 5548	24,28	49679–50008	0.01718	72.5	$21.7^{+2.6}_{-2.6}$	43.604 ± 0.012	43.436 ± 0.026	41.746 ± 0.013	6946 ± 79	2432 ± 13	2247 ± 134
NGC 5548	24,28	50044–50373	0.01718	72.5	$16.4^{+1.2}_{-1.1}$	43.527 ± 0.020	43.317 ± 0.039	41.656 ± 0.018	6623 ± 93	2276 ± 15	2026 ± 68
NGC 5548	24,29	50434–50729	0.01718	72.5	$17.5^{+2.0}_{-1.6}$	43.413 ± 0.018	43.113 ± 0.054	41.622 ± 0.015	6298 ± 65	2178 ± 12	1923 ± 62
NGC 5548	24,29	50775–51085	0.01718	72.5	$26.5^{+4.3}_{-2.2}$	43.620 ± 0.020	43.459 ± 0.032	41.762 ± 0.018	6177 ± 36	2035 ± 11	1732 ± 76
NGC 5548	24,29	51142–51456	0.01718	72.5	$24.8^{+3.2}_{-3.0}$	43.565 ± 0.017	43.376 ± 0.034	41.719 ± 0.016	6247 ± 57	2021 ± 18	1980 ± 30
NGC 5548	24,29	51517–51791	0.01718	72.5	$6.5^{+5.7}_{-3.7}$	43.327 ± 0.019	42.918 ± 0.081	41.521 ± 0.017	6240 ± 77	2010 ± 30	1969 ± 48
NGC 5548	24,29	51878–52174	0.01718	72.5	$14.3^{+5.9}_{-7.3}$	43.321 ± 0.027	42.903 ± 0.089	41.428 ± 0.026	6478 ± 108	3111 ± 131	2173 ± 89
NGC 5548	24,30	53432–53472	0.01718	72.5	$6.3^{+2.6}_{-2.3}$	43.263 ± 0.016	42.526 ± 0.211	40.967 ± 0.017	6396 ± 167	3210 ± 642	2388 ± 373
NGC 5548	10,24	54180–54332	0.01718	72.5	$12.4^{+2.7}_{-3.9}$	43.287 ± 0.008	42.665 ± 0.140	40.660 ± 0.070	12575 ± 47	4736 ± 23	1822 ± 35
NGC 5548	11,24	54508–54618	0.01718	72.5	$4.18^{+0.86}_{-1.30}$	43.214 ± 0.010	42.621 ± 0.129	41.157 ± 0.017	12771 ± 71	4266 ± 65	4270 ± 292
NGC 5548	8,24	55931–56072	0.01718	72.5	$2.83^{+0.88}_{-0.90}$	43.433 ± 0.005	43.070 ± 0.058	41.543 ± 0.010	10587 ± 82	3056 ± 4	2772 ± 34
NGC 5548	31	56663–56875	0.01718	72.5	$4.17^{+0.36}_{-0.36}$	43.612 ± 0.003	43.404 ± 0.027	41.666 ± 0.004	9496 ± 418	3691 ± 162	4278 ± 671
NGC 5548	32	57030–57236	0.01718	72.5	$7.18^{+1.38}_{-0.70}$	43.175 ± 0.005	42.787 ± 0.063	41.630 ± 0.003	9912 ± 362	3350 ± 272	3124 ± 302
PG 1426+015	3	48334–51042	0.08657	383.9	$95.0^{+29.9}_{-37.1}$	44.690 ± 0.012	44.568 ± 0.019	42.764 ± 0.015	7113 ± 160	2906 ± 80	3442 ± 308
Mrk 817	1	49000–49212	0.03146	134.2	$19.0^{+3.9}_{-3.7}$	43.848 ± 0.010	43.726 ± 0.015	42.010 ± 0.010	4711 ± 78	1984 ± 8	1392 ± 78
Mrk 817	1	49404–49528	0.03146	134.2	$15.3^{+3.7}_{-3.5}$	43.761 ± 0.087	43.608 ± 0.124	41.936 ± 0.089	5237 ± 67	2098 ± 13	1971 ± 96

Table A1
(Continued)

Source	References	JD Range (−2,400,000)	z	D_L (Mpc)	$\tau(\mathrm{H}\beta)$ (days)	$\log L_{\mathrm{total}}(5100)$ (erg s^{-1})	$\log L_{\mathrm{AGN}}(5100)$ (erg s^{-1})	$\log L(\mathrm{H}\beta_{\mathrm{broad}})$ (erg s^{-1})	$\mathrm{FWHM_M}(\mathrm{H}\beta)$ (km s^{-1})	$\sigma_{\mathrm{M}}(\mathrm{H}\beta)$ (km s^{-1})	$\sigma_{\mathrm{R}}(\mathrm{H}\beta)$ (km s^{-1})
(1)	(2)	(3)	(4)	(5)	(6)	(7)	(8)	(9)	(10)	(11)	(12)
Mrk 817	1	49752–49924	0.03146	134.2	$33.6^{+6.5}_{-7.6}$	43.762 ± 0.009	43.609 ± 0.016	41.860 ± 0.010	4767 ± 72	2195 ± 16	1729 ± 158
Mrk 817	10	54185–54301	0.03146	134.2	$14.04^{+3.41}_{-3.47}$	43.901 ± 0.006	43.776 ± 0.010	41.710 ± 0.016	5906 ± 34	2365 ± 9	2025 ± 5
Mrk 290	10	54180–54321	0.02958	126.0	$8.72^{+1.21}_{-1.02}$	43.451 ± 0.028	43.157 ± 0.036	41.747 ± 0.030	4521 ± 24	2071 ± 24	1609 ± 47
PG 1613+658	3	48397–51073	0.12900	588.4	$40.1^{+15.0}_{-15.2}$	44.948 ± 0.010	44.713 ± 0.019	42.943 ± 0.014	9074 ± 103	3084 ± 33	2547 ± 342
PG 1617+175	3	48362–51085	0.11244	507.4	$71.5^{+29.6}_{-33.7}$	44.445 ± 0.011	44.330 ± 0.014	42.682 ± 0.023	6641 ± 190	2313 ± 69	2626 ± 211
PG 1700+518	3	48378–51084	0.29200	1463.3	$251.8^{+45.9}_{-38.8}$	45.600 ± 0.010	45.528 ± 0.011	43.717 ± 0.020	2252 ± 85	3160 ± 93	1700 ± 123
3C 382	6	56679–56864	0.05787	251.5	$40.49^{+8.02}_{-3.74}$	44.193 ± 0.008	43.792 ± 0.069	42.264 ± 0.011	3619 ± 203	3227 ± 7	4552 ± 190
3C 390.3	33	49718–50012	0.05610	243.5	$23.60^{+6.2}_{-6.7}$	43.902 ± 0.018	43.620 ± 0.039	42.222 ± 0.015	12694 ± 13	3744 ± 42	3105 ± 81
3C 390.3	34	50100–54300	0.05610	243.5	$97.0^{+17.0}_{-17.0}$	44.028 ± 0.016	43.913 ± 0.020	42.287 ± 0.021	11918 ± 325	…	…
3C 390.3	35	53631–53714	0.05610	243.5	$46.4^{+3.8}_{-3.2}$	44.485 ± 0.007	44.434 ± 0.008	42.695 ± 0.012	13211 ± 278	5377 ± 37	5455 ± 278
NGC 6814	11	54545–54618	0.00521	21.6	$6.64^{+0.87}_{-0.90}$	42.500 ± 0.017	42.058 ± 0.057	40.443 ± 0.010	3323 ± 7	1918 ± 36	1610 ± 108
Mrk 509	1	47653–50374	0.03440	147.0	$79.6^{+6.1}_{-5.4}$	44.240 ± 0.027	44.130 ± 0.028	42.545 ± 0.027	3015 ± 2	1555 ± 7	1276 ± 28
PG 2130+099	36	54352–54450	0.06298	274.7	$22.9^{+4.7}_{-4.6}$	44.406 ± 0.012	44.368 ± 0.012	42.667 ± 0.011	2853 ± 39	1485 ± 15	1246 ± 222
PG 2130+099	2	55430–55557	0.06298	274.7	$9.6^{+1.2}_{-1.2}$	44.237 ± 0.032	44.150 ± 0.033	42.584 ± 0.033	1781 ± 5	1769 ± 2	1825 ± 65
NGC 7469	37	55430–55568	0.01632	68.8	$10.8^{+3.4}_{-1.3}$	43.768 ± 0.009	43.444 ± 0.051	41.557 ± 0.013	4369 ± 6	1095 ± 5	1274 ± 126

Note. Column (1): AGN name. Column (2): literature reference for data. Column (3): Julian Dates of observations. Column (4): redshift. Column (5): luminosity distance. Column (6): Hβ time lag. Column (7): log total luminosity at 5100 Å. Column (8): log AGN luminosity at 5100 Å. Column (9): log Hβ broad-line component luminosity. Column (10): FWHM of Hβ broad component in mean spectrum. Column (11): line dispersion of Hβ broad component in mean spectrum. Column (12): line dispersion of Hβ broad component in rms spectrum.

References. (1) Peterson et al. 1998a; (2) Grier et al. 2012; (3) Kaspi et al. 2000; (4) Santos-Lleó et al. 1997; (5) Kollatschny et al. 2014; (6) Fausnaugh et al. 2017; (7) Doroshenko et al. 2012; (8) De Rosa et al. 2018; (9) Kollatschny et al. 2001; (10) Denney et al. 2010; (11) Bentz et al. 2009b; (12) Du et al. 2014; (13) Bentz et al. 2008; (14) Stirpe et al. 1994; (15) Onken & Peterson 2002; (16) Denney et al. 2009b; (17) Bentz et al. 2006a; (18) Zhang et al. 2019; (19) Denney et al. 2006; (20) Bentz et al. 2016; (21) Bentz et al. 2014; (22) Santos-Lleó et al. 2001; (23) Peterson et al. 1991; (24) Peterson et al. 2013; (25) Peterson et al. 1992; (26) Peterson et al. 1994; (27) Korista et al. 1995; (28) Peterson et al. 1999; (29) Peterson et al. 2002; (30) Bentz et al. 2007; (31) Pei et al. 2017; (32) Lu et al. 2016; (33) Dietrich et al. 1998; (34) Shapovalova et al. 2010; (35) Dietrich et al. 2012; (36) Grier et al. 2008; (37) Peterson et al. 2014.

Table A2
Reverberation-mapped AGNs (C IV)

Source	References	JD Range (−2,400,000)	z	D_L (Mpc)	τ(C IV) (days)	log L(1350) (erg s^{-1})	FWHM$_M$(C IV) (km s^{-1})	σ_M(C IV) (km s^{-1})	σ_R(C IV) (km s^{-1})
(1)	(2)	(3)	(4)	(5)	(6)	(7)	(8)	(9)	(10)
DES J003–42	1	56919–57627	2.593	20723	123^{+43}_{-42}	46.510 ± 0.020	4944 ± 93	3917 ± 29	6250 ± 64
Fairall 9	2,3	49473–49713	0.04702	202.8	$29.6^{+12.9}_{-14.4}$	44.530 ± 0.030	2968 ± 37	3068 ± 27	3201 ± 285
DES J228–04	1	56919–57627	1.905	1686.4	95^{+16}_{-23}	46.430 ± 0.098	5232 ± 57	3932 ± 22	6365 ± 66
CT 286	4	54821–57759	2.556	20,366	459^{+71}_{-92}	46.798 ± 0.009	6256	…	…
CT 406	4	54355–57605	3.183	26,533	115^{+64}_{-86}	46.910 ± 0.040	6236	…	…
NGC 3783	5,3	48611–48833	0.00973	25.1	$3.8^{+1.0}_{-0.9}$	43.081 ± 0.017	2784 ± 24	2476 ± 18	2948 ± 160
NGC 4151	6,7	47494–47556	0.00332	15.0	$3.44^{+1.42}_{-1.24}$	42.412 ± 0.016	2929 ± 154	4922 ± 51	5426 ± 196
NGC 4395	8	53106	0.00106	4.0	$0.033^{+0.017}_{-0.013}$	39.494 ± 0.007	1214 ± 2	1727 ± 78	3025 ± 201
NGC 4395	8	53190	0.00106	4.0	$0.046^{+0.017}_{-0.013}$	40.030 ± 0.012	1532 ± 6	1662 ± 34	2859 ± 376
NGC 5548	9,3	47510–47745	0.01718	72.5	$9.8^{+1.9}_{-1.5}$	43.635 ± 0.016	5248 ± 428	4351 ± 37	3842 ± 210
NGC 5548	10,3	49060–49135	0.01718	72.5	$6.7^{+0.9}_{-1.0}$	43.552 ± 0.007	4201 ± 101	3738 ± 17	3328 ± 104
NGC 5548	11	56690–56866	0.01718	72.5	$5.8^{+0.5}_{-0.5}$	43.625 ± 0.007	5236 ± 87	2205 ± 16	2075 ± 81
3C 390.3	12,3	49718–50147	0.05610	243.5	$35.7^{+11.4}_{-14.6}$	44.013 ± 0.045	6180 ± 638	4578 ± 65	4400 ± 186
J214355	4	54729–57605	2.620	20,985	128^{+91}_{-82}	46.962 ± 0.048	6895	…	…
J221516	4	54232–57689	2.706	21821	165^{+98}_{-13}	47.155 ± 0.057	5888	…	…
NGC 7469	13,3	50245–50293	0.01632	68.8	$2.5^{+0.3}_{-0.3}$	43.719 ± 0.016	3112 ± 54	3650 ± 27	2619 ± 118

Note. Column (1): AGN name. Column (2): literature reference for data. Column (3): Julian Dates of observations. Column (4): redshift. Column (5): luminosity distance. Column (6): C IV time lag τ(C IV). Column (7): log continuum luminosity at 1350 Å. Column (8): FWHM of C IV in the mean spectrum. Column (9): line dispersion of C IV in the mean spectrum. Column (10): line dispersion of C IV in the rms spectrum.
References. (1) Hoormann et al. 2019; (2) Rodríguez-Pascual et al. 1997; (3) Peterson et al. 2004; (4) Lira et al. 2018; (5) Reichert et al. 1994; (6) Clavel et al. 1990; (7) Metzroth et al. 2006; (8) Peterson et al. 2005; (9) Clavel et al. 1991; (10) Korista et al. 1995; (11) De Rosa et al. 2015; (12) O'Brien et al. 1998; (13) Wanders et al. 1997.

Table A3
Reverberation-mapped AGNs (SDSS Hβ)

RMID	z	D_L (Mpc)	τ(Hβ) (days)	log L(5100) (erg s^{-1})	log L(Hβ_{broad}) (erg s^{-1})	FWHM$_M$(Hβ) (km s^{-1})	σ_M(Hβ) (km s^{-1})	σ_R(Hβ) (km s^{-1})
(1)	(2)	(3)	(4)	(5)	(6)	(7)	(8)	(9)
16	0.848	5240.9	$32.0^{+11.6}_{-15.5}$	44.7779 ± 0.0012	43.0718 ± 0.0600	7042 ± 43	4804 ± 41	6477 ± 54
17	0.456	2466.9	$25.5^{+10.9}_{-5.8}$	44.3552 ± 0.0005	42.1756 ± 0.0064	7847 ± 203	4295 ± 47	6101 ± 48
101	0.458	2479.8	$21.4^{+4.2}_{-6.4}$	44.3758 ± 0.0005	42.7316 ± 0.0449	2207 ± 7	1178 ± 5	976 ± 32
160	0.359	1859.7	$21.9^{+4.2}_{-2.4}$	43.7613 ± 0.0009	42.0456 ± 0.0047	3988 ± 23	2914 ± 36	1909 ± 12
177	0.482	2635.8	$10.1^{+12.5}_{-2.7}$	44.1735 ± 0.0009	42.2813 ± 0.0125	4808 ± 32	2224 ± 32	2036 ± 39
191	0.442	2377.0	$8.5^{+2.5}_{-1.4}$	43.9111 ± 0.0015	41.7344 ± 0.0131	2023 ± 32	1078 ± 79	1030 ± 18
229	0.47	2557.5	$16.2^{+2.9}_{-4.5}$	43.8259 ± 0.0017	41.9083 ± 0.0166	3089 ± 261	2178 ± 156	1781 ± 38
265	0.734	4388.8	$8.5^{+3.2}_{-3.9}$	44.3809 ± 0.0019	42.4400 ± 0.0273	3655 ± 323	2526 ± 55	7165 ± 36
267	0.587	3342.0	$20.4^{+2.5}_{-2.0}$	44.3013 ± 0.0008	42.5166 ± 0.0237	2395 ± 23	1229 ± 32	1202 ± 33
272	0.263	1298.0	$15.1^{+3.2}_{-4.6}$	43.9119 ± 0.0009	42.3449 ± 0.0017	2595 ± 10	1590 ± 5	1697 ± 10
300	0.646	3754.6	$30.4^{+3.9}_{-8.3}$	44.6130 ± 0.0008	42.5889 ± 0.0379	2376 ± 33	1303 ± 29	1232 ± 30
305	0.527	2933.9	$53.5^{+4.2}_{-4.0}$	44.2995 ± 0.0008	42.5025 ± 0.0365	2208 ± 28	1647 ± 20	2126 ± 35
316	0.676	3968.3	$11.9^{+1.3}_{-1.0}$	44.9958 ± 0.0004	43.4279 ± 0.0020	2988 ± 10	1884 ± 5	7195 ± 40
320	0.265	1309.4	$25.2^{+4.7}_{-5.7}$	43.6876 ± 0.0010	41.8663 ± 0.0096	4061 ± 26	3110 ± 37	1462 ± 26
371	0.472	2570.5	$13^{+1.4}_{-0.8}$	44.0638 ± 0.0009	42.3726 ± 0.0086	3506 ± 26	1682 ± 18	1443 ± 11
373	0.884	5516.4	$20.4^{+5.6}_{-7.0}$	44.9025 ± 0.0012	42.7743 ± 0.0191	5987 ± 268	1897 ± 48	2491 ± 26
377	0.337	1727.4	$5.9^{+0.4}_{-0.6}$	43.7819 ± 0.0011	41.5130 ± 0.0156	2746 ± 118	1576 ± 23	1789 ± 23
392	0.843	5202.8	$14.2^{+3.7}_{-3.0}$	44.4249 ± 0.0032	42.4894 ± 0.0427	2419 ± 82	2446 ± 110	3658 ± 56
399	0.608	3487.6	$35.8^{+1.1}_{-10.3}$	44.3272 ± 0.0020	42.2823 ± 0.0281	2689 ± 88	1989 ± 89	1619 ± 38
428	0.976	6233.7	$15.8^{+6.0}_{-1.9}$	45.4013 ± 0.0015	43.2816 ± 0.0048	2795 ± 29	1836 ± 18	7568 ± 70
551	0.68	3997.0	$6.4^{+1.5}_{-1.4}$	44.1196 ± 0.0021	42.4389 ± 0.0842	2101 ± 45	1255 ± 59	1298 ± 36
589	0.751	4513.8	$46^{+9.5}_{-9.5}$	44.4877 ± 0.0015	42.6421 ± 0.0107	3738 ± 62	2835 ± 62	5013 ± 49
622	0.572	3238.9	$49.1^{+11.1}_{-2.0}$	44.3737 ± 0.0006	42.5966 ± 0.0062	2389 ± 36	1147 ± 11	1423 ± 32
645	0.474	2583.6	$20.7^{+0.9}_{-3.0}$	44.1342 ± 0.0008	42.2965 ± 0.0047	6428 ± 163	2799 ± 13	1438 ± 17
720	0.467	2538.0	$41.6^{+14.8}_{-8.3}$	44.3176 ± 0.0008	42.4324 ± 0.0029	2829 ± 15	1679 ± 17	1232 ± 16
772	0.249	1219.6	$3.9^{+0.9}_{-0.9}$	43.7867 ± 0.0005	41.5251 ± 0.0081	2381 ± 33	1983 ± 40	1026 ± 14
775	0.172	805.9	$16.3^{+13.1}_{-6.6}$	43.7943 ± 0.0003	41.7848 ± 0.0021	2744 ± 36	2028 ± 10	1818 ± 8

Table A3
(Continued)

RMID	z	D_L (Mpc)	τ(Hβ) (days)	log L(5100) (erg s^{-1})	log L(H$\beta_{\rm broad}$) (erg s^{-1})	FWHM$_{\rm M}$(Hβ) (km s^{-1})	$\sigma_{\rm M}$(Hβ) (km s^{-1})	$\sigma_{\rm R}$(Hβ) (km s^{-1})
(1)	(2)	(3)	(4)	(5)	(6)	(7)	(8)	(9)
776	0.116	524.6	$10.5^{+1.0}_{-2.2}$	43.3829 ± 0.0004	41.4179 ± 0.0220	3060 ± 20	3178 ± 19	1409 ± 11
781	0.263	1298.0	$75.2^{+3.2}_{-3.3}$	43.7604 ± 0.0034	41.8863 ± 0.0155	2506 ± 19	1290 ± 17	1089 ± 22
782	0.362	1877.9	$20^{+1.1}_{-3.0}$	44.0941 ± 0.0006	41.9722 ± 0.0044	3027 ± 35	1527 ± 16	1353 ± 23
790	0.237	1153.2	$5.5^{+5.7}_{-2.1}$	43.8222 ± 0.0014	41.8443 ± 0.0272	8365 ± 44	5069 ± 47	6318 ± 38
840	0.244	1191.8	$5^{+1.5}_{-1.4}$	43.6987 ± 0.0005	41.5724 ± 0.0074	6116 ± 267	3286 ± 254	4457 ± 60

Note. Column (1): reverberation-mapping identifier (see Shen et al. 2015). Column (2): redshift. Column (3): luminosity distance. Column (4): Hβ time lag. Column (5): log AGN continuum luminosity at 5100 Å. Column (6): log broad Hβ luminosity. Column (7): FWHM of Hβ in the mean spectrum. Column (8): line dispersion of Hβ in the mean spectrum. Column (9): line dispersion of Hβ in the rms spectrum.

Table A4
Reverberation-mapped AGNs (SDSS C IV)

RMID	z	D_L (Mpc)	τ(C IV) (days)	log L(1350 Å) (erg s^{-1})	FWHM$_{\rm M}$(C IV) (km s^{-1})	$\sigma_{\rm M}$(C IV) (km s^{-1})	$\sigma_{\rm R}$(C IV) (km s^{-1})
(1)	(2)	(3)	(4)	(5)	(6)	(7)	(8)
0	1.463	10283	$131.1^{+42.9}_{-36.6}$	44.847 ± 0.004	3967 ± 107	1968 ± 160	2144 ± 46
32	1.72	12554	$22.8^{+3.5}_{-3.6}$	44.492 ± 0.021	2999 ± 34	1770 ± 24	2017 ± 10
36	2.213	17094	$188.4^{+15.6}_{-29}$	45.909 ± 0.001	4830 ± 24	2890 ± 24	3900 ± 34
52	2.311	18020	$56.5^{+3.1}_{-5.9}$	45.499 ± 0.002	2258 ± 14	1809 ± 15	1322 ± 22
57	1.93	14461	$208.3^{+10.6}_{-5.6}$	45.393 ± 0.003	2692 ± 11	1626 ± 8	1682 ± 12
58	2.299	17906	$186.1^{+5.9}_{-7.4}$	45.353 ± 0.002	3627 ± 45	2611 ± 31	3412 ± 30
130	1.96	14737	$224.3^{+12.4}_{-37.9}$	45.534 ± 0.001	5619 ± 30	4078 ± 55	4324 ± 36
144	2.295	17868	$179.4^{+31.2}_{-42.3}$	45.516 ± 0.001	6153 ± 53	2762 ± 19	2792 ± 19
145	2.138	16390	$180.9^{+4.7}_{-4.7}$	45.113 ± 0.004	4472 ± 74	3287 ± 40	3408 ± 16
158	1.477	10405	$36.7^{+18.6}_{-26.1}$	44.999 ± 0.004	3603 ± 101	2099 ± 60	2136 ± 31
161	2.071	15764	$180.1^{+5.6}_{-6.4}$	45.491 ± 0.001	3163 ± 28	2323 ± 25	2524 ± 20
181	1.678	12177	$102.6^{+5}_{-10.1}$	44.545 ± 0.015	2998 ± 35	2127 ± 44	2721 ± 34
201	1.797	13248	$41.3^{+32}_{-19.5}$	46.240 ± 0.001	5438 ± 56	1833 ± 9	2408 ± 117
231	1.646	11892	$80.4^{+6.3}_{-7.5}$	45.736 ± 0.001	5975 ± 98	3267 ± 102	3803 ± 18
237	2.394	18810	$49.9^{+6.6}_{-4.4}$	45.866 ± 0.001	5455 ± 39	2734 ± 18	2779 ± 23
245	1.677	12168	$107.1^{+22.9}_{-28.6}$	45.351 ± 0.004	9496 ± 107	4174 ± 54	3953 ± 86
249	1.721	12562	$24.9^{+9.7}_{-3.1}$	44.984 ± 0.010	1871 ± 15	1432 ± 12	1640 ± 15
256	2.247	17414	$43^{+16.3}_{-11.9}$	45.089 ± 0.003	2544 ± 54	1742 ± 29	1802 ± 24
269	2.4	18868	$197.2^{+2.4}_{-12.6}$	45.193 ± 0.003	3930 ± 312	3280 ± 50	3547 ± 30
275	1.58	11307	$81^{+8.2}_{-24.4}$	45.611 ± 0.001	3213 ± 20	2108 ± 9	2406 ± 5
295	2.351	18400	$163.8^{+8.2}_{-5.3}$	45.605 ± 0.001	4311 ± 41	2501 ± 23	2446 ± 19
298	1.633	11777	$106.1^{+18.7}_{-31.7}$	45.596 ± 0.001	3160 ± 30	2066 ± 26	2549 ± 35
312	1.929	14452	$56.9^{+11.4}_{-6.7}$	45.077 ± 0.004	7663 ± 166	4273 ± 74	4291 ± 30
332	2.58	20598	$81.6^{+5.6}_{-11.4}$	45.551 ± 0.002	3799 ± 14	3009 ± 63	4277 ± 33
346	1.592	11413	$71.9^{+23.8}_{-11.3}$	44.905 ± 0.003	3389 ± 168	2220 ± 131	3055 ± 29
386	1.862	13838	$38.2^{+13.2}_{-19.3}$	45.279 ± 0.002	2972 ± 40	1782 ± 38	2187 ± 41
387	2.427	19126	$30.3^{+19.6}_{-3.4}$	45.687 ± 0.001	3676 ± 24	2123 ± 14	2451 ± 23
389	1.851	13738	$224.3^{+7.1}_{-18}$	45.564 ± 0.002	5222 ± 111	3839 ± 16	4064 ± 15
401	1.823	13484	$47.4^{+15.2}_{-8.9}$	45.564 ± 0.002	3273 ± 21	2457 ± 12	3321 ± 12
411	1.734	12679	$248.3^{+21.1}_{-39}$	44.887 ± 0.007	4256 ± 67	2511 ± 61	2490 ± 39
418	1.419	9903	$82.5^{+27.6}_{-16.9}$	45.040 ± 0.003	3143 ± 44	2662 ± 94	3110 ± 23
470	1.883	14030	$19.9^{+43.2}_{-4}$	44.821 ± 0.006	4022 ± 52	2441 ± 34	2317 ± 60
485	2.557	20376	$133.4^{+22.6}_{-5.2}$	46.119 ± 0.001	5342 ± 48	2924 ± 32	3961 ± 41
496	2.079	15839	$197.9^{+9.7}_{-6.6}$	45.560 ± 0.001	2364 ± 27	2137 ± 34	2409 ± 45
499	2.327	18172	$168.5^{+20.4}_{-35.9}$	45.058 ± 0.003	3261 ± 41	2968 ± 41	3085 ± 26
506	1.753	12850	$231.6^{+13.3}_{-11.1}$	45.075 ± 0.003	5046 ± 52	3507 ± 27	3510 ± 24
527	1.651	11937	$52.3^{+15.1}_{-12.2}$	44.788 ± 0.003	5154 ± 110	3384 ± 62	3587 ± 34
549	2.277	17698	$69.8^{+5.3}_{-7.2}$	45.369 ± 0.002	3907 ± 59	1818 ± 47	2176 ± 21
554	1.707	12437	$194^{+20.4}_{-12.2}$	45.573 ± 0.002	3690 ± 65	2253 ± 47	2229 ± 35

Table A4
(Continued)

RMID	z	D_L (Mpc)	τ(C IV) (days)	$\log L$(1350 Å) (erg s^{-1})	FWHM$_M$(C IV) (km s^{-1})	σ_M(C IV) (km s^{-1})	σ_R(C IV) (km s^{-1})
(1)	(2)	(3)	(4)	(5)	(6)	(7)	(8)
562	2.773	22476	$158.5^{+18.2}_{-34.2}$	46.302 ± 0.001	4379 ± 113	2036 ± 29	2078 ± 27
686	2.13	16315	$64.7^{+12.6}_{-6.3}$	45.444 ± 0.002	3827 ± 34	2135 ± 25	2203 ± 27
689	2.007	15170	$157.6^{+22.9}_{-42.2}$	45.223 ± 0.003	2258 ± 23	1292 ± 8	1407 ± 5
734	2.324	18144	$87.2^{+13.9}_{-11}$	45.530 ± 0.001	5701 ± 121	2982 ± 65	3405 ± 40
809	1.67	12106	$108.6^{+27.7}_{-50.7}$	45.204 ± 0.005	4811 ± 38	5210 ± 60	4749 ± 96
827	1.966	14792	$137.7^{+18.3}_{-19.4}$	44.999 ± 0.006	2542 ± 35	971 ± 13	1443 ± 13

Note. Column (1): reverberation-mapping identifier (see Shen et al. 2015). Column (2): redshift. Column (3): luminosity distance. Column (4): C IV time lag. Column (5): log continuum luminosity at 1350 Å. Column (6): FWHM of C IV in the mean spectrum. Column (7): line dispersion of C IV in the mean spectrum. Column (8): line dispersion of C IV in the rms spectrum.

Table A5
C IV Single-Epoch Masses (VP06)

Source	FWHM$_M$(C IV) (km s^{-1})	σ_M(C IV) (km s^{-1})	$\log L$(1350) (erg s^{-1})	μ_{SE}(VP06) ($M_\odot$)	μ_{SE}(SDSS-RM) ($M_\odot$)
(1)	(2)	(3)	(4)	(5)	(6)
Mrk 335	2291 ± 27	2116 ± 160	44.173 ± 0.020	6.663 ± 0.337	7.079 ± 0.145
Mrk 335	1741 ± 99	1806 ± 360	44.291 ± 0.078	6.588 ± 0.375	7.080 ± 0.187
Mrk 335	2023 ± 17	2140 ± 93	44.262 ± 0.013	6.720 ± 0.332	7.153 ± 0.140
PG 0026+129	1837 ± 136	3364 ± 70	45.165 ± 0.025	7.591 ± 0.331	8.092 ± 0.140
PG 0052+251	3983 ± 370	5118 ± 486	45.265 ± 0.037	8.009 ± 0.341	8.402 ± 0.150
PG 0052+251	5192 ± 251	5083 ± 437	45.176 ± 0.041	7.956 ± 0.339	8.331 ± 0.149
Fairall 9	2593 ± 65	2981 ± 197	44.470 ± 0.028	7.118 ± 0.335	7.496 ± 0.144
Fairall 9	2831 ± 40	3532 ± 92	44.582 ± 0.011	7.325 ± 0.331	7.676 ± 0.139
Fairall 9	2370 ± 151	2978 ± 508	44.759 ± 0.126	7.270 ± 0.368	7.715 ± 0.193
Mrk 590	4839 ± 59	3574 ± 141	44.119 ± 0.029	7.089 ± 0.332	7.330 ± 0.141
3C 120	3302 ± 75	3199 ± 169	44.943 ± 0.039	7.430 ± 0.334	7.895 ± 0.144
3C 120	3278 ± 105	3409 ± 286	44.617 ± 0.056	7.312 ± 0.339	7.682 ± 0.152
Ark 120	3989 ± 451	3795 ± 165	44.634 ± 0.021	7.414 ± 0.332	7.755 ± 0.141
Ark 120	3945 ± 42	3240 ± 149	44.482 ± 0.022	7.197 ± 0.333	7.551 ± 0.141
Mrk 79	3182 ± 521	3344 ± 222	43.879 ± 0.039	6.904 ± 0.336	7.110 ± 0.146
Mrk 79	3049 ± 128	2971 ± 248	43.495 ± 0.058	6.598 ± 0.339	6.752 ± 0.152
Mrk 79	3113 ± 122	3803 ± 388	43.726 ± 0.065	6.935 ± 0.343	7.065 ± 0.157
Mrk 110	2990 ± 64	2601 ± 272	43.770 ± 0.050	6.628 ± 0.343	6.887 ± 0.155
Mrk 110	1638 ± 59	2576 ± 231	43.876 ± 0.081	6.676 ± 0.342	6.962 ± 0.159
PG 0953+414	2873 ± 57	3512 ± 361	45.588 ± 0.031	7.853 ± 0.342	8.438 ± 0.151
NGC 3516	4675 ± 538	3311 ± 372	42.830 ± 0.093	6.340 ± 0.348	6.306 ± 0.167
NGC 3516	4875 ± 17	3132 ± 64	42.823 ± 0.017	6.288 ± 0.331	6.270 ± 0.139
NGC 3516	5147 ± 103	3245 ± 84	43.192 ± 0.013	6.514 ± 0.331	6.570 ± 0.139
NGC 3516	4729 ± 28	3430 ± 92	43.143 ± 0.013	6.536 ± 0.331	6.564 ± 0.139
NGC 3516	4525 ± 97	3137 ± 79	43.030 ± 0.012	6.399 ± 0.331	6.428 ± 0.139
NGC 3516	3940 ± 18	2834 ± 95	42.485 ± 0.034	6.022 ± 0.332	5.957 ± 0.142
NGC 3516	4912 ± 23	3973 ± 36	42.793 ± 0.012	6.479 ± 0.330	6.380 ± 0.138
NGC 3783	2831 ± 22	3273 ± 100	43.601 ± 0.014	6.738 ± 0.331	6.886 ± 0.139
NGC 3783	2308 ± 17	3179 ± 185	43.744 ± 0.022	6.789 ± 0.334	6.979 ± 0.143
NGC 4051	1319 ± 13	1713 ± 227	41.373 ± 0.058	4.995 ± 0.351	4.830 ± 0.163
NGC 4151	6929 ± 76	5220 ± 123	43.224 ± 0.010	6.944 ± 0.331	6.860 ± 0.139
NGC 4151	5418 ± 150	4604 ± 249	43.340 ± 0.019	6.896 ± 0.333	6.878 ± 0.142
NGC 4151	5062 ± 51	4651 ± 371	43.396 ± 0.029	6.935 ± 0.338	6.926 ± 0.147
NGC 4151	5246 ± 44	4675 ± 397	43.396 ± 0.031	6.939 ± 0.339	6.929 ± 0.148
NGC 4151	5752 ± 144	4585 ± 321	43.418 ± 0.023	6.934 ± 0.336	6.935 ± 0.144
NGC 4151	5173 ± 593	4664 ± 475	43.354 ± 0.044	6.915 ± 0.342	6.896 ± 0.153
NGC 4151	3509 ± 10	4384 ± 66	43.038 ± 0.006	6.694 ± 0.330	6.621 ± 0.138
PG 1229+204	3391 ± 205	3241 ± 457	44.654 ± 0.028	7.288 ± 0.352	7.682 ± 0.160
PG 1307+085	3465 ± 168	3687 ± 290	45.012 ± 0.039	7.590 ± 0.338	8.027 ± 0.148
Mrk 279	4126 ± 487	3118 ± 414	43.795 ± 0.118	6.799 ± 0.355	7.007 ± 0.181
Mrk 279	3876 ± 99	3286 ± 511	43.754 ± 0.127	6.823 ± 0.363	7.005 ± 0.189
NGC 5548	4790 ± 67	4815 ± 257	43.654 ± 0.022	7.102 ± 0.333	7.142 ± 0.142
NGC 5548	4096 ± 14	3973 ± 34	43.568 ± 0.006	6.889 ± 0.330	6.969 ± 0.138

Table A5
(Continued)

Source	$FWHM_M$(C IV) (km s^{-1})	σ_M(C IV) (km s^{-1})	$\log L(1350)$ (erg s^{-1})	μ_{SE}(VP06) ($M_\odot$)	μ_{SE}(SDSS-RM) ($M_\odot$)
(1)	(2)	(3)	(4)	(5)	(6)
NGC 5548	3280 ± 27	5050 ± 787	43.773 ± 0.069	7.206 ± 0.359	7.259 ± 0.171
PG 1426+015	3778 ± 448	4101 ± 391	45.295 ± 0.023	7.832 ± 0.340	8.301 ± 0.149
Mrk 817	4027 ± 71	4062 ± 289	44.123 ± 0.022	7.203 ± 0.336	7.404 ± 0.145
PG 1613+658	5902 ± 136	3965 ± 215	45.221 ± 0.023	7.764 ± 0.334	8.226 ± 0.142
PG 1617+175	4558 ± 1763	3383 ± 1036	44.784 ± 0.108	7.394 ± 0.428	7.805 ± 0.234
Mrk 509	5035 ± 298	3558 ± 205	44.641 ± 0.029	7.362 ± 0.334	7.725 ± 0.143
Mrk 509	4345 ± 49	3426 ± 115	44.532 ± 0.015	7.272 ± 0.331	7.621 ± 0.140
Mrk 509	4973 ± 233	3647 ± 172	44.803 ± 0.020	7.469 ± 0.333	7.862 ± 0.141
Mrk 509	4961 ± 218	3127 ± 226	44.552 ± 0.033	7.203 ± 0.336	7.585 ± 0.146
Mrk 509	3716 ± 228	3174 ± 448	44.706 ± 0.071	7.297 ± 0.354	7.710 ± 0.168
PG 2130+099	2113 ± 119	2390 ± 184	44.692 ± 0.025	7.044 ± 0.337	7.541 ± 0.146
NGC 7469	3094 ± 53	3379 ± 182	43.774 ± 0.016	6.858 ± 0.333	7.036 ± 0.142
NGC 7469	2860 ± 12	3266 ± 110	43.679 ± 0.015	6.778 ± 0.331	6.945 ± 0.140

Note. Data sources are listed in Table 2 of VP06. Column (1): AGN name. Column (2): FWHM of C IV. Column (3): line dispersion of C IV. Column (4): AGN continuum luminosity at 1350 Å. Column (5): single-epoch virial product from VP06. Column (6): single-epoch virial product based on the data in this table and Equation (42).

ORCID iDs

Elena Dalla Bontà https://orcid.org/0000-0001-9931-8681
Bradley M. Peterson https://orcid.org/0000-0001-6481-5397
Misty C. Bentz https://orcid.org/0000-0002-2816-5398
W. N. Brandt https://orcid.org/0000-0002-0167-2453
S. Ciroi https://orcid.org/0000-0001-9539-3940
Gisella De Rosa https://orcid.org/0000-0003-3242-7052
Gloria Fonseca Alvarez https://orcid.org/0000-0003-0042-6936
Catherine J. Grier https://orcid.org/0000-0001-9920-6057
P. B. Hall https://orcid.org/0000-0002-1763-5825
Juan V. Hernández Santisteban https://orcid.org/0000-0002-6733-5556
Luis C. Ho https://orcid.org/0000-0001-6947-5846
Y. Homayouni https://orcid.org/0000-0002-0957-7151
Keith Horne https://orcid.org/0000-0003-1728-0304
C. S. Kochanek https://orcid.org/0000-0001-6017-2961
Jennifer I-Hsiu Li https://orcid.org/0000-0002-0311-2812
L. Morelli https://orcid.org/0000-0001-6890-3503
A. Pizzella https://orcid.org/0000-0001-9585-417X
R. W. Pogge https://orcid.org/0000-0003-1435-3053
D. P. Schneider https://orcid.org/0000-0001-7240-7449
Yue Shen https://orcid.org/0000-0003-1659-7035
J. R. Trump https://orcid.org/0000-0002-1410-0470
Marianne Vestergaard https://orcid.org/0000-0001-9191-9837

References

Allen, J. T., Hewett, P. C., Maddox, N., et al. 2011, MNRAS, 410, 860
Antonucci, R. R. J., & Cohen, R. D. 1983, ApJ, 271, 564
Assef, R. J., Denney, K. D., Kochanek, C. S., et al. 2011, ApJ, 742, 93
Bahk, H., Woo, J.-H., & Park, D. 2019, ApJ, 875, 50
Baldwin, J. A. 1977, ApJ, 214, 679
Barth, A. J., Bennert, V. N., Canalizo, G., et al. 2015, ApJS, 217, 26
Baskin, A., & Laor, A. 2004, MNRAS, 350, L31
Baskin, A., & Laor, A. 2005, MNRAS, 356, 1029
Batiste, M., Bentz, M. C., Raimundo, S. I., Vestergaard, M., & Onken, C. A. 2017, ApJL, 838, L10
Bentz, M. C., Cackett, E. M., Crenshaw, D. M., et al. 2016, ApJ, 830, 136
Bentz, M. C., Denney, K. D., Cackett, E. M., et al. 2006a, ApJ, 651, 775
Bentz, M. C., Denney, K. D., Cackett, E. M., et al. 2007, ApJ, 662, 205
Bentz, M. C., Denney, K. D., Grier, C. J., et al. 2013, ApJ, 767, 149
Bentz, M. C., Ferrarese, L., Onken, C. A., Peterson, B. M., & Valluri, M. 2019, ApJ, 885, 161
Bentz, M. C., Horenstein, D., Bazhaw, C., et al. 2014, ApJ, 796, 8
Bentz, M. C., & Katz, S. 2015, PASP, 127, 67
Bentz, M. C., Peterson, B. M., Netzer, H., Pogge, R. W., & Vestergaard, M. 2009a, ApJ, 697, 160
Bentz, M. C., Peterson, B. M., Pogge, R. W., Vestergaard, M., & Onken, C. A. 2006b, ApJ, 644, 133
Bentz, M. C., Walsh, J. L., Barth, A. J., et al. 2008, ApJL, 689, L21
Bentz, M. C., Walsh, J. L., Barth, A. J., et al. 2009b, ApJ, 705, 199
Bentz, M. C., Walsh, J. L., Barth, A. J., et al. 2010, ApJ, 726, 993
Bian, W.-H., Fang, L.-L., Huang, K.-L., & Wang, J.-M. 2012, MNRAS, 427, 2881
Bisogni, S., di Serego Alighieri, S., Goldoni, P., et al. 2017, A&A, 603, A1
Blandford, R. D., & McKee, C. F. 1982, ApJ, 255, 419
Boller, Th., Brandt, W. N., & Fink, H. 1996, A&A, 305, 53
Boroson, T. A. 2002, ApJ, 565, 78
Boroson, T. A., & Green, R. F. 1992, ApJS, 80, 109
Brotherton, M. S., Runnoe, J. C., Shang, Z., & DiPompeo, M. A. 2015a, MNRAS, 451, 1290
Brotherton, M. S., Singh, V., & Runnoe, J. 2015b, MNRAS, 454, 3864
Burbidge, G., & Burbidge, M. 1967, Quasi-Stellar Objects (San Francisco: Freeman)
Cackett, E. M., Gültekin, K., Bentz, M. C., et al. 2015, ApJ, 810, 86
Cackett, E. M., & Horne, K. 2006, MNRAS, 365, 1180
Cappellari, M., Scott, N., Alatalo, K., et al. 2013, MNRAS, 432, 1709
Clavel, J., Boksenberg, A., Bromage, G. E., et al. 1990, MNRAS, 246, 668
Clavel, J., Reichert, G. A., Alloin, D., et al. 1991, ApJ, 366, 64
Clavel, J., Wamsteker, W., & Glass, I. S. 1989, ApJ, 337, 236
Coatman, L., Hewett, P. C., Banerji, M., et al. 2016, MNRAS, 461, 647
Coatman, L., Hewett, P. C., Banerji, M., et al. 2017, MNRAS, 465, 2120
Collin, S., Kawaguchi, T., Peterson, B. M., & Vestergaard, M. 2006, A&A, 456, 75
Corbett, E. A., Croom, S. M., Boyle, B. J., et al. 2003, MNRAS, 343, 705
Corbin, M. R. 1990, ApJ, 357, 346
Czerny, B., Olejak, A., Rałowski, M., et al. 2019, ApJ, 880, 46
Dalla Bontà, E., Davies, R. L., Houghton, R. C. W., et al. 2018, MNRAS, 474, 339
Davidson, K. 1972, ApJ, 171, 213
Davidson, K., & Netzer, H. 1979, RvMP, 51, 715
De Rosa, G., Fausnaugh, M. M., Grier, C. J., et al. 2018, ApJ, 866, 133
De Rosa, G., Peterson, B. M., Ely, J., et al. 2015, ApJ, 806, 128
Denney, K. D. 2012, ApJ, 759, 44
Denney, K. D., Bentz, M. C., Peterson, B. M., et al. 2006, ApJ, 653, 152
Denney, K. D., Peterson, B. M., Dietrich, M., Vestergaard, M., & Bentz, M. C. 2009a, ApJ, 692, 246

Denney, K. D., Peterson, B. M., Pogge, R. W., et al. 2010, ApJ, 721, 715
Denney, K. D., Pogge, R. W., Assef, R. J., et al. 2013, ApJ, 775, 60
Denney, K. D., Watson, L. C., Peterson, B. M., et al. 2009b, ApJ, 702, 1353
Dibai, E. A. 1980, SvA, 24, 389
Dietrich, M., Peterson, B. M., Albrecht, P., et al. 1998, ApJS, 115, 185
Dietrich, M., Peterson, B. M., Grier, C. J., et al. 2012, ApJ, 757, 53
Doroshenko, V. T., Sergeev, S. G., Klimanov, S. A., Pronik, V. I., & Efimov, Y. S. 2012, MNRAS, 426, 416
Du, P., Hu, C., Lu, K.-X., et al. 2014, ApJ, 782, 45
Du, P., Lu, K.-X., Zhang, Z.-X., et al. 2016, ApJ, 825, 126
Du, P., & Wang, J.-M. 2019, ApJ, 886, 42
Du, P., Zhang, Z.-X., Wang, K., et al. 2018, ApJ, 856, 6
Edelson, R., Gelbord, J., Cackett, E., et al. 2017, ApJ, 840, 41
Edelson, R., Gelbord, J., Cackett, E., et al. 2019, ApJ, 870, 123
Edelson, R., Gelbord, J. M., Horne, K., et al. 2015, ApJ, 806, 129
Espey, B. R., Carswell, R. F., Bailey, J. A., et al. 1989, ApJ, 342, 666
Fausnaugh, M. M., Denney, K. D., Barth, A. J., et al. 2016, ApJ, 821, 56
Fausnaugh, M. M., Grier, C. J., Bentz, M. C., et al. 2017, ApJ, 840, 97
Ferland, G. J., & Shields, G. A. 1985, in Astrophysics of Active Galaxies and Quasi-Stellar Objects, ed. J. S. Miller (Mill Valley, CA: Univ. Science Books), 157
Ferrarese, L., & Merritt, D. 2000, ApJL, 539, L9
Fine, S., Croom, S. M., Hopkins, P. F., et al. 2008, MNRAS, 390, 1413
Fonseca Alvarez, G., Trump, J. R., Homayouni, Y., et al. 2020, ApJ, 899, 73
Fromerth, M. J., & Melia, F. 2000, ApJ, 533, 172
Gaskell, C. M. 1982, ApJ, 263, 79
Gaskell, C. M., & Peterson, B. M. 1987, ApJS, 65, 1
Gebhardt, K., Bender, R., Bower, G., et al. 2000, ApJL, 539, L13
Gilbert, K. M., & Peterson, B. M. 2003, ApJ, 587, 123
Goad, M. R., Korista, K. T., & Knigge, C. 2004, MNRAS, 352, 277
Greene, J. E., & Ho, L. C. 2005, ApJ, 630, 122
Greene, J. E., & Ho, L. C. 2007, ApJ, 667, 131
Greene, J. E., Hood, C. E., Barth, A. J., et al. 2010, ApJ, 723, 409
Greene, J. E., Peng, C. Y., & Ludwig, R. R. 2010, ApJ, 709, 937
Grier, C. J., Martini, P., Watson, L. C., et al. 2013, ApJ, 773, 90
Grier, C. J., Pancoast, A., Barth, A. J., et al. 2017a, ApJ, 849, 146
Grier, C. J., Peterson, B. M., Bentz, M. C., et al. 2008, ApJ, 688, 837
Grier, C. J., Peterson, B. M., Pogge, R. W., et al. 2012, ApJ, 755, 60
Grier, C. J., Shen, Y., Horne, K., et al. 2019, ApJ, 887, 38
Grier, C. J., Trump, J. R., Shen, Y., et al. 2017b, ApJ, 851, 21, Erratum: 2018, ApJ, 868:76
Gültekin, K., Richstone, D. O., Gebhardt, K., et al. 2009, ApJ, 698, 198
Hall, P. B., Anderson, S. F., Strauss, M. A., et al. 2002, ApJS, 141, 267
Hewett, P. C., & Foltz, C. B. 2003, AJ, 125, 1784
Homayouni, Y., Trump, J. R., Grier, C. J., et al. 2020, ApJ, 901, 55
Hoormann, J. K., Martini, P., Davis, T. M., et al. 2019, MNRAS, 487, 3650
Ilić, D., Shapovalova, A. I., Popović, L. Č., et al. 2017, FrASS, 4, 12
Joly, M., Collin-Souffrin, S., Masnou, J. L., & Nottale, L. 1985, A&A, 152, 282
Kaspi, S., Brandt, W. N., Maoz, D., et al. 2007, ApJ, 659, 997
Kaspi, S., Maoz, D., Netzer, H., et al. 2005, ApJ, 629, 61
Kaspi, S., Smith, P. S., Netzer, H., et al. 2000, ApJ, 533, 631
Kollatschny, W. 2003, A&A, 407, 461
Kollatschny, W., Bischoff, K., Robinson, E. L., Welsh, W. F., & Hill, G. J. 2001, A&A, 379, 125
Kollatschny, W., Ulbrich, K., Zetzl, M., Kaspi, S., & Haas, M. 2014, A&A, 566, A106
Kollatschny, W., & Zetzl, M. 2013, A&A, 549, A100
Kollmeier, J. A., Onken, C. A., Kochanek, C. S., et al. 2006, ApJ, 648, 128
Koratkar, A. P., & Gaskell, C. M. 1991, ApJL, 370, L61
Korista, K., Baldwin, J., & Ferland, G. 1998, ApJ, 507, 24
Korista, K. T., Alloin, D., Barr, P., et al. 1995, ApJS, 97, 285
Krolik, J. H., Horne, K., Kallman, T. R., et al. 1991, ApJ, 371, 541
Laor, A. 1998, ApJL, 505, L83
Li, J. I., Shen, Y., Brandt, W. N., et al. 2019, ApJ, 884, 119
Lira, P., Kaspi, S., Netzer, H., et al. 2018, ApJ, 865, 56
Lu, K.-X., Du, P., Hu, C., et al. 2016, ApJ, 827, 118
Marconi, A., Axon, D. J., Maiolino, R., et al. 2008, ApJ, 678, 693
Marconi, A., Axon, D. J., Maiolino, R., et al. 2009, ApJL, 698, L103
Martínez-Aldama, M. L., Czerny, B., Kawka, D., et al. 2019, ApJ, 883, 170
Martínez-Aldama, M. L., Zajaček, M., Czerny, B., & Panda, S. 2020, arXiv:2007.09955
Marziani, P., del Olmo, A., Martínez-Carballo, M. A., et al. 2019, A&A, 627, A88
Marziani, P., Dultzin, D., Sulentic, J. W., et al. 2018, FrASS, 5, 6
McHardy, I. M., Cameron, D. T., Dwelly, T., et al. 2014, MNRAS, 444, 1469
McHardy, I. M., Connolly, S. D., Horne, K., et al. 2018, MNRAS, 480, 2881
McLure, R. J., & Jarvis, M. J. 2002, MNRAS, 337, 109
Mejía-Restrepo, J. E., Trakhtenbrot, B., Lira, P., et al. 2018, MNRAS, 478, 1929
Metzroth, K. G., Onken, C. A., & Peterson, B. M. 2006, ApJ, 647, 901
Netzer, H. 2019, MNRAS, 488, 5185
Netzer, H., Lira, P., Trakhtenbrot, B., et al. 2007, ApJ, 671, 1256
Netzer, H., & Marziani, P. 2010, ApJ, 724, 318
O'Brien, P. T., Dietrich, M., Leighly, K., et al. 1998, ApJ, 509, 163
Onken, C. A., & Peterson, B. M. 2002, ApJ, 572, 746
Osterbrock, D. E. 1985, in Astrophysics of Active Galaxies and Quasi-Stellar Objects, ed. J. S. Miller (Mill Valley, CA: Univ. Science Books), 111
Osterbrock, D. E., & Pogge, R. W. 1985, ApJ, 297, 166
Padovani, P., & Rafanelli, P. 1988, A&A, 205, 53
Pancoast, A., Brewer, B. J., Treu, T., et al. 2014, MNRAS, 445, 3073
Park, D., Barth, A. J., Woo, J.-H., et al. 2017, ApJ, 839, 93
Pei, L., Fausnaugh, M. M., Barth, A. J., et al. 2017, ApJ, 837, 131
Peterson, B. M. 1993, PASP, 105, 247
Peterson, B. M. 2014, SSRv, 183, 253
Peterson, B. M., Alloin, D., Axon, D., et al. 1992, ApJ, 392, 470
Peterson, B. M., Balonek, T. J., Barker, E. S., et al. 1991, ApJ, 368, 119
Peterson, B. M., Barth, A. J., Berlind, P., et al. 1999, ApJ, 510, 659
Peterson, B. M., Bentz, M. C., Desroches, L.-B., et al. 2005, ApJ, 632, 799
Peterson, B. M., Berlind, P., Bertram, R., et al. 1994, ApJ, 425, 622
Peterson, B. M., Berlind, P., Bertram, R., et al. 2002, ApJ, 581, 197
Peterson, B. M., Denney, K. D., De Rosa, G., et al. 2013, ApJ, 779, 109
Peterson, B. M., Ferrarese, L., Gilbert, K. M., et al. 2004, ApJ, 613, 682
Peterson, B. M., Grier, C. J., Horne, K., et al. 2014, ApJ, 795, 149
Peterson, B. M., Meyers, K. A., Capriotti, E. R., et al. 1985, ApJ, 292, 164
Peterson, B. M., & Wandel, A. 1999, ApJL, 521, L95
Peterson, B. M., & Wandel, A. 2000, ApJL, 540, L13
Peterson, B. M., Wanders, I., Bertram, R., et al. 1998a, ApJ, 501, 82
Peterson, B. M., Wanders, I., Horne, K., et al. 1998b, PASP, 110, 660
Phillips, M. M. 1978, ApJS, 38, 187
Pogge, R. W., & Peterson, B. M. 1992, AJ, 103, 1084
Rafiee, A., & Hall, P. B. 2011, MNRAS, 415, 2932
Reichert, G. A., Rodriguez-Pascual, P. M., Alloin, D., et al. 1994, ApJ, 425, 582
Richards, G. T., Kruczek, N. E., Gallagher, S. C., et al. 2011, AJ, 141, 167
Richards, G. T., Vanden Berk, D. E., Reichard, T. A., et al. 2002, AJ, 124, 1
Rodríguez-Pascual, P. M., Alloin, D., Clavel, J., et al. 1997, ApJS, 110, 9
Rousseeuw, P., & van Driessen, K. 2006, Data Min. Knowl. Discovery, 12, 29
Runnoe, J. C., Brotherton, M. S., Shang, Z., & DiPompeo, M. A. 2013a, MNRAS, 434, 848
Runnoe, J. C., Brotherton, M. S., Shang, Z., Wills, B. J., & DiPompeo, M. A. 2013b, MNRAS, 429, 135
Santos-Lleó, M., Chatzichristou, E., de Oliveira, C. M., et al. 1997, ApJS, 112, 271
Santos-Lleó, M., Clavel, J., Schulz, B., et al. 2001, A&A, 369, 57
Schlafly, E. F., & Finkbeiner, D. P. 2011, ApJ, 737, 103
Schlegel, D. J., Finkbeiner, D. P., & Davis, M. 1998, ApJ, 500, 525
Shapovalova, A. I., Popović, L. Č., Burenkov, A. N., et al. 2010, A&A, 517, A42
Shappee, B. J., Prieto, J. L., Grupe, D., et al. 2014, ApJ, 788, 48
Shen, J., Vanden Berk, D. E., Schneider, D. P., et al. 2008a, AJ, 135, 928
Shen, Y. 2013, BASI, 41, 61
Shen, Y. 2016, ApJ, 817, 55
Shen, Y., Brandt, W. N., Dawson, K. S., et al. 2015, ApJS, 216, 4
Shen, Y., Greene, J. E., Strauss, M. A., et al. 2008b, ApJ, 680, 169
Shen, Y., Hall, P. B., Horne, K., et al. 2019, ApJS, 241, 34
Shen, Y., & Ho, L. C. 2014, Natur, 513, 210
Shen, Y., Horne, K., Grier, C. J., et al. 2016, ApJ, 818, 30
Shen, Y., & Kelly, B. C. 2012, ApJ, 746, 169
Shen, Y., & Liu, X. 2012, ApJ, 753, 125
Steinhardt, C. L., & Elvis, M. 2010, MNRAS, 402, 2637
Stirpe, G. M., Winge, C., Altieri, B., et al. 1994, ApJ, 425, 609
Sulentic, J. W., Bachev, R., Marziani, P., et al. 2007, ApJ, 666, 757
Sulentic, J. W., del Olmo, A., Marziani, P., et al. 2017, A&A, 608, A122
Sulentic, J. W., Zwitter, T., Marziani, P., & Dultzin-Hacyan, D. 2000, ApJL, 536, L5
Sun, J., & Shen, Y. 2015, ApJL, 804, L15
Tarter, C. B., & McKee, C. F. 1973, ApJL, 186, L63
Trakhtenbrot, B., & Netzer, H. 2012, MNRAS, 427, 3081

Trevese, D., Perna, M., Vagnetti, F., Saturni, F. G., & Dadina, M. 2014, ApJ, 795, 164
Vanden Berk, D. E., Yip, C., Connolly, A., Jester, S., & Stoughton, C. 2004, in ASP Conf. Ser. 311, AGN Physics with the Sloan Digital Sky Survey, ed. G. T. Richards & P. B. Hall (San Francisco, CA: ASP), 21
Vestergaard, M. 2002, ApJ, 571, 733
Vestergaard, M. 2004, ApJ, 601, 676
Vestergaard, M., Fan, X., Tremonti, C. A., et al. 2008, ApJL, 674, L1
Vestergaard, M., & Peterson, B. M. 2006, ApJ, 641, 689
Vietri, G., Piconcelli, E., Bischetti, M., et al. 2018, A&A, 617, A81
Wandel, A., Peterson, B. M., & Malkan, M. A. 1999, ApJ, 526, 579
Wandel, A., & Yahil, A. 1985, ApJL, 295, L1
Wanders, I., Peterson, B. M., Alloin, D., et al. 1997, ApJS, 113, 69
Wang, S., Shen, Y., Jiang, L., et al. 2019, ApJ, 882, 4
Wang, S., Shen, Y., Jiang, L., et al. 2020, ApJ, in press (arXiv:2006.06178)
Weedman, D. W. 1976, QJRAS, 17, 227
Weymann, R. J., Morris, S. L., Foltz, C. B., et al. 1991, ApJ, 373, 23
White, R. J., & Peterson, B. M. 1994, PASP, 106, 879
Wilkes, B. J. 1984, MNRAS, 207, 73
Wilkes, B. J. 1986, MNRAS, 218, 331
Wills, B. J., Brotherton, M. S., Fang, D., et al. 1993, ApJ, 415, 563
Wills, B. J., & Browne, I. W. A. 1986, ApJ, 302, 56
Woltjer, L. 1959, ApJ, 130, 38
Woo, J.-H., Schulze, A., Park, D., et al. 2013, ApJ, 772, 49
Yee, H. K. C. 1980, ApJ, 241, 894
Yu, Z., Kochanek, C. S., Peterson, B. M., et al. 2020, MNRAS, 491, 6045
Zajaček, M., Czerny, B., Martínez-Aldama, M. L., et al. 2020, ApJ, 896, 146
Zhang, Z.-X., Du, P., Smith, P. S., et al. 2019, ApJ, 876, 49
Zu, Y., Kochanek, C. S., & Peterson, B. M. 2011, ApJ, 735, 80